Simulation of turbulent flow over idealized water waves

By PETER P. SULLIVAN[1], JAMES C. McWILLIAMS[1,2]
AND CHIN-HOH MOENG[1]

[1]National Center for Atmospheric Research, Boulder, Colorado 80307, USA,

[2]Department of Atmospheric Sciences and Institute of Geophysics and Planetary Physics, UCLA, Los Angeles, CA 90095, USA

Turbulent flow over idealized water waves with varying wave slope ak and wave age c/u_* is investigated using direct numerical simulations at a bulk Reynolds number $Re = 8000$. In the present idealization, the shape of the water wave and the associated orbital velocities are prescribed and do not evolve dynamically under the action of the wind. The results show that the imposed waves significantly influence the mean flow, vertical momentum fluxes, velocity variances, pressure, and form stress (drag). Compared to a stationary wave, slow (fast) moving waves increase (decrease) the form stress. At small c/u_*, waves act similarly to increasing surface roughness z_o resulting in mean vertical velocity profiles with shorter buffer and longer logarithmic regions. With increasing wave age, z_o decreases so that the wavy lower surface is nearly as smooth as a flat lower boundary. Vertical profiles of turbulence statistics show that the wave effects depend on wave age and wave slope but are confined to a region $kz < 1$ (where k is the wavenumber of the surface undulation and z is the vertical coordinate). The turbulent momentum flux can be altered by as much as 40% by the waves. A region of closed streamlines (or cat's-eye pattern) centred about the critical layer height was found to be dynamically important at low to moderate values of c/u_*. The wave-correlated velocity and flux fields are strongly dependent on the variation of the critical layer height and to a lesser extent the surface orbital velocities. Above the critical layer z_{cr} the positions of the maximum and minimum wave-correlated vertical velocity w_w occur upwind and downwind of the peak in z_{cr}, like a stationary surface. The wave-correlated flux $u_w w_w$ is positive (negative) above (below) the critical layer height.

1. Introduction

The interaction between atmospheric turbulence and water waves is of considerable importance in geophysical flows. Wind-generated waves influence the flux of momentum and scalars at the air–sea interface and represent a visible signature of coupling between the atmosphere and ocean. Also, the fundamental difference between atmospheric boundary layers over land and water derives from the scale and mobility of the water surface. Despite extensive past work, the present understanding of the physical mechanisms at work in turbulent air flow over waves remains unclear, partly because of the formidable difficulties of obtaining and interpreting field observations over the open ocean (e.g. Edson & Fairall 1998 and Hristov, Friehe & Miller 1998). From the perspective of the atmospheric boundary layer, questions persist as

to the influence of ocean waves on the height of the wave-induced boundary layer, the partitioning of the vertical momentum flux between turbulent and wave-induced components, the modification of Monin–Obukhov similarity theory, the role wave age plays in the determination of surface drag, and the parameterization of wave effects for large-scale numerical models.

The uncertainty about fundamental aspects of wind–wave interaction is illustrated by the wide scatter (more than a factor of 2) in the variation of wave growth with wave age deduced from field observations (e.g. see Gent & Taylor 1976, figure 11). The current generation of numerical models based on Reynolds-averaged equations and eddy viscosity prescriptions (e.g. Gent & Taylor 1976; Gent 1977; Harris & Street 1994; Harris, Belcher & Street 1996; Mastenbroek *et al.* 1996; Li 1995) also predict wide variations in important parameters like wave growth depending on the type of turbulence closure scheme adopted (Belcher & Hunt 1998 provide a recent review). As noted by Harris *et al.* (1996) there is compelling evidence to suggest that there are multiple physical parameters, like surface roughness (Gent & Taylor 1976), influencing wave growth. The commonly accepted view in geophysical flows over land surfaces assumes that the surface roughness is sufficiently large that the fluid dynamics is independent of Reynolds number. However, Kitaigorodskii & Donelan (1984) and Harris *et al.* (1996) point out that the Reynolds number is likely to be important since oceanic conditions are often either transitional or even smooth rather than fully rough, thus further adding to the complexity of wind–wave interaction.

The goal of the present work is to develop and use three-dimensional, time-dependent direct numerical simulations to examine turbulent air flow over water waves thus eliminating dependence on turbulence closure assumptions. Numerical simulations of turbulent flows have become an important tool for studying the basic physics of turbulent flows (for reviews see Rogallo & Moin 1984 and Moin & Mahesh 1998), but are not commonly applied to flows with complex boundaries. Access to time-dependent, three-dimensional datasets allows the spatial and temporal evolution of turbulent flow fields to be examined in detail that is not routinely available to the experimentalist. Because of the complexity of the wind–wave problem, in this paper we only consider the direct numerical simulation (DNS) of turbulent flow, admittedly at low Reynolds number, over idealized water waves. The specific objective is to identify wave effects on the turbulent flow above a moving wavy surface as a function of wave age.

There have been a few studies using DNS as well as large-eddy simulation (LES) to examine turbulent flows over complex geometry, like wavy surfaces. Henn & Sykes (1999), Cherukat *et al.* (1998), De Angelis, Lombardi & Banerjee (1997), and Maass & Schumann (1994) consider turbulent flow over sinusoidal surfaces driven by a pressure gradient, i.e. channel flow. Gong, Taylor & Dornbrack (1996) use LES to simulate turbulent flow developing over sinusoidal waves in a wind tunnel, and Choi, Moin & Kim (1992) employ DNS to study turbulent flow over streamwise oriented riblets. Also, Krettenauer & Schumann (1992) consider turbulent convection over wavy terrain utilizing DNS. It is important to mention that in all of these studies, the wavy boundary is *stationary* and thus not applicable to flow over water waves. Caponi *et al.* (1982) consider moving wavy surfaces of finite amplitude but the calculations assume two-dimensional laminar viscous flow.

For the present study, we examine the effects of a moving wavy surface on plane turbulent Couette flow, rather than pressure-driven channel flow. This choice is motivated by the fact that the mean total vertical flux (or stress) in Couette flow is constant with height independent of the flow state (i.e. laminar, transitional or
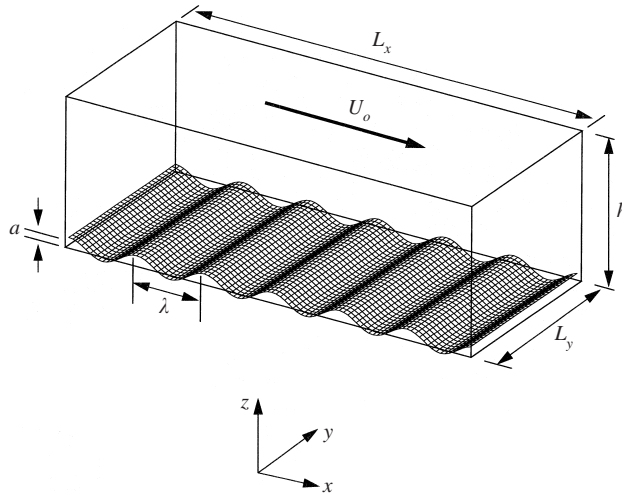
FIGURE 1. Sketch of three-dimensional Couette flow driven by velocity U_o over a moving wavy boundary of wavelength λ (or wavenumber $k = 2\pi/\lambda$), phase speed c, and amplitude a in a domain of size $(L_x, L_y, h) = (6, 5, 1)\lambda$. For clarity, the surface grid is shown with less resolution than actually used in the computations.

turbulent). Secondly, Komminaho, Lundbladh & Johansson (1996) point out that the limiting near-wall values in Couette flow are closer to those of higher Reynolds number flow in channels and boundary layers. Turbulent Couette flow differs from pressure-driven channel flow because the total stress (or flux) is constant vertically, the mean flow pressure gradient is identically zero, the mean horizontal velocity profile is monotonic, there is finite turbulence production at all z, and large-scale coherent structures have been found in the central region of the channel (e.g. Lee & Kim 1991). There are relatively few experimental investigations of plane turbulent Couette flow because of practical difficulties associated with establishing the flow in the laboratory. A discussion of numerical simulations and experimental studies of plane turbulent Couette flow over flat boundaries is provided by Papavassiliou & Hanratty (1997), Komminaho *et al.* (1996), Bech *et al.* (1995), and Aydin & Leutheusser (1991).

2. Problem formulation

2.1. *Flow configuration*

The problem considered is three-dimensional plane turbulent Couette flow over two-dimensional water waves. A sketch showing the flow orientation, coordinate system, and the wavy lower boundary is given in figure 1. We adopt a coordinate system where x is aligned with the primary flow direction, y is parallel to the wave crests and z is measured vertically from the mean water surface. In our idealization, the water wave is assumed to be a two-dimensional, periodic (in x), non-evolving, deep-water gravity wave of wavelength λ, phase speed c, amplitude a, and wave slope $ak = a2\pi/\lambda$. Typically, the wave slope is small but finite, i.e. $ak < 0.1$. The orbital velocities at the water surface, which are included in the surface boundary conditions (see §2.5), are assumed to be given by first-order wave theory. For our computations and analysis, the frame of reference is travelling with the waves, i.e. $x = x' - ct$, where t is time and x' is an absolute coordinate. In (x, y, z) coordinates the water surface displacements and orbital velocities are independent of time. The domain size

is $(L_x, L_y, h) = (6, 5, 1)\lambda$ and the air flow is assumed to be periodic in the horizontal directions (x, y). A large-scale constant velocity U_o imposed at $z = h$ drives the flow. The wall friction velocity u_* is based on the constant total stress τ_w, i.e. $u_* = (\tau_w/\rho)^{1/2}$, where ρ is the fluid density.

2.2. *Governing equations*

The flow field is assumed to satisfy the conservation equations for mass and momentum for an incompressible fluid with density ρ and kinematic viscosity v. In Cartesian coordinates x_i $(i = 1, 2, 3) = (x, y, z)$ a dimensionless form for the set of governing equations is

$$\frac{\partial u_i}{\partial x_i} = 0, \tag{2.1}$$

$$\frac{\partial u_i}{\partial t} + \frac{\partial u_i u_j}{\partial x_j} = -\frac{\partial p}{\partial x_i} + \frac{1}{Re} \frac{\partial^2 u_i}{\partial x_j \partial x_j}, \tag{2.2}$$

where u_i $(i = 1, 2, 3) = (u, v, w)$ are Cartesian velocity components and p is the pressure. Velocity, length, time, and pressure are non-dimensionalized by $U_o, h, h/U_o$, and ρU_o^2, respectively. The bulk Reynolds number is $Re = U_o h/v$. The wave properties, namely c, a, λ, k and the wall friction velocity u_*, which appear in the later discussion, are also made dimensionless by U_o and h.

2.3. *Coordinate transformation*

The strategy is to transform just the coordinates in the governing equations into a surface-fitted curvilinear system applicable to flow over two-dimensional moving water waves. Simple conformal (and thus orthogonal) transformations exist which will map the physical domain in figure 1 on to a flat computational domain. The specialization of the mapping to a conformal transformation is not viewed as a severe restriction in the present study as it minimizes the number of additional new terms in the transformed equations (and hence the computational requirements), but still permits adequate control over the grid spacing. Furthermore, pseudoconformal transformations allow for arbitrary two-dimensional geometries that are periodic in one direction (Mobely & Stewart 1980) which is the situation considered in the present work.

We adopt the two-dimensional conformal mapping proposed by Benjamin (1959) with the obvious extension to three dimensions

$$\begin{bmatrix} \xi \\ \eta \\ \zeta \end{bmatrix} = \begin{bmatrix} x - iae^{-kz}e^{ikx} \\ y \\ z - ae^{-kz}e^{ikx} \end{bmatrix} \tag{2.3}$$

where (ξ, η, ζ) are surface-fitted coordinates and (ξ, ζ) are roughly aligned with the Cartesian (x, z) coordinates. Only the real part of (2.3) is to be considered. The actual boundary wave shape z_{bdy}, obtained by setting $\zeta = 0$ in (2.3) and retaining first-order terms in ak, is

$$z_{bdy}(x) \approx a \cos kx(1 - ak \cos kx). \tag{2.4}$$

The lower boundary shape departs from a pure sinusoidal waveform with increasing ak, producing flatter crests and deeper troughs. However, we investigate small values of ak (see §5) and the deviations from a pure sinusoidal shape are small. In the physical plane, the vertical oscillation of a ξ-line rapidly diminishes with increasing

z because of the exponential dependence in (2.3); the vertical variation of the upper boundary grid line ($kz = 2\pi$) is much less than 0.1% and thus is considered uniform.

The metric elements connecting the Cartesian and curvilinear systems expressed as functions of (x, y, z) are (subscripts here denote partial differentiation)

$$\begin{bmatrix} \xi_x & \xi_y & \xi_z \\ \eta_x & \eta_y & \eta_z \\ \zeta_x & \zeta_y & \zeta_z \end{bmatrix} = \begin{bmatrix} 1 + ake^{-kz}e^{ikx} & 0 & iake^{-kz}e^{ikx} \\ 0 & 1 & 0 \\ -iake^{-kz}e^{ikx} & 0 & 1 + ake^{-kz}e^{ikx} \end{bmatrix}. \tag{2.5}$$

The coordinate transformation satisfies the Cauchy–Riemann conditions $\partial\xi/\partial x = \partial\zeta/\partial z$ and $\partial\xi/\partial z = -\partial\zeta/\partial x$, and therefore the Jacobian is

$$J = \frac{\partial\xi}{\partial x}\frac{\partial\zeta}{\partial z} - \frac{\partial\xi}{\partial z}\frac{\partial\zeta}{\partial x} = \left(\frac{\partial\xi}{\partial x}\right)^2 + \left(\frac{\partial\xi}{\partial z}\right)^2. \tag{2.6}$$

2.4. *Governing equations in transformed coordinates*

Using the chain rule, the set of governing equations (2.1) and (2.2) is next written in surface-fitted coordinates ξ_i ($i = 1, 2, 3) = (\xi, \eta, \zeta)$ as

$$\frac{\partial U_i}{\partial \xi_i} = 0, \tag{2.7}$$

$$\frac{1}{J}\frac{\partial u_i}{\partial t} = -\frac{\partial}{\partial\xi_j}U_j u_i - \frac{\partial}{\partial\xi_j}\left(\frac{p}{J}\frac{\partial\xi_j}{\partial x_i}\right) + \frac{1}{Re}\left(\frac{\partial^2 u_i}{\partial\xi\partial\xi} + \frac{\partial^2 u_i}{\partial\zeta\partial\zeta} + \frac{1}{J}\frac{\partial^2 u_i}{\partial\eta\partial\eta}\right), \tag{2.8}$$

where the fundamental unknowns are the Cartesian velocity components u_i and pressure p. These equations are expressed in so-called strong conservation form (e.g. Anderson, Tannehill & Pletcher 1984, p. 254) by using the identity

$$\frac{\partial}{\partial\xi_j}\left(\frac{1}{J}\frac{\partial\xi_j}{\partial x_i}\right) = 0. \tag{2.9}$$

We have explicitly inserted the metric elements for an arbitrary two-dimensional conformal transformation into the viscous term of (2.8) which simplifies its appearance. The continuity equation and the advective terms in the momentum equations are expressed in terms of contravariant 'flux' velocities U_i ($i = 1, 2, 3) = (U, V, W)$ defined by

$$U_i = \frac{u_j}{J}\frac{\partial\xi_i}{\partial x_j}. \tag{2.10}$$

As a consequence of these contravariant flux velocities, the advective terms in transformed coordinates retain a similar structure to their counterparts in (x, y, z) coordinates.

2.5. *Boundary conditions*

The boundary conditions are chosen consistent with a direct numerical simulation that resolves viscous wall layers along the upper and lower boundaries in figure 1, while in horizontal planes periodic boundary conditions are assumed. Since the frame of reference is moving with the wave phase speed c, the dimensionless boundary conditions for the Cartesian and contravariant flux velocities at the upper boundary ($\zeta = 1$) are

$$\begin{bmatrix} u & v & w \\ JU & JV & JW \end{bmatrix} = \begin{bmatrix} 1 - c & 0 & 0 \\ (1 - c)\xi_x & 0 & (1 - c)\zeta_x \end{bmatrix}. \tag{2.11}$$
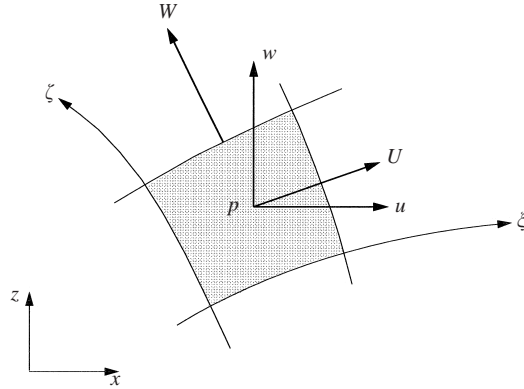
FIGURE 2. Location of Cartesian velocity components (u, w), contravariant flux velocities (U, W), and pressure p in a two-dimensional (ξ, ζ) plane for the mixed finite-difference pseudospectral differencing scheme. Cartesian and flux velocities (v, V) aligned with the spanwise coordinate (y, η) (not shown) are also located at cell centres.

At the upper boundary $(\xi_x, \xi_z, J) \to (1, 0, 1)$ and hence $(U, V, W) \to (1 - c, 0, 0)$ because of the exponential dependence in (2.5).

At the lower boundary, the velocity components are matched to the first-order (in ak) irrotational orbital velocities for a two-dimensional deep-water gravity wave (Lighthill 1978)

$$(u, v, w)_{bdy} = akc \left(\cos k[x' - ct], 0, \sin k[x' - ct] \right). \qquad (2.12)$$

Thus, at $\zeta = 0$ the velocity boundary conditions, in the frame of reference moving with the waves, are

$$\begin{bmatrix} u & v & w \\ JU & JV & JW \end{bmatrix} = \begin{bmatrix} c(-1 + ak \cos kx) & 0 & akc \sin kx \\ -c & 0 & 0 \end{bmatrix}, \qquad (2.13)$$

where we have approximated the metric elements by $\xi_x \approx 1 + ak \cos kx$ and $\xi_z \approx -ak \sin kx$. In the situation $c = 0$, the lower boundary conditions reduce to the familiar no-slip conditions.

It should be noted that the governing equations and boundary conditions described above are nonlinear and not fundamentally limited to small wave slope ak although for the present study $ak \ll 1$. In this particular aspect, the set of equations differs from many second-order closure models (e.g. Harris *et al.* 1996; Li 1995) that first introduce a coordinate transformation and then a perturbation expansion in powers of ak for the field variables.

3. Numerical method

The numerical method used to solve the system of equations (2.7) and (2.8) with boundary conditions (2.11) and (2.13) builds on our prior successful experience with LES of geophysical flows (Moeng 1984; Sullivan, McWilliams & Moeng 1996; and McWilliams, Sullivan & Moeng 1997) and the co-located grid architecture described by Zang, Street & Koseff (1994). In order to accommodate curved, non-stationary boundaries our usual LES staggered grid arrangement is replaced by a cell-centred (or co-located) arrangement for all variables as shown in figure 2. Centred schemes, commonplace in the engineering community (e.g. Ferziger & Perić 1996), are ad-

vantageous since large boundary slopes can be easily treated and the differencing stencil is the same for all variables. The crucial idea of the co-located scheme is to evaluate all forces at cell centres for calculating the velocity tendency, but interpolate the forces to the cell faces to enforce the continuity equation through the calculation of pressure from the divergence of the momentum equations. This mimics a three-dimensional staggered grid arrangement, and the pressure and velocity fields remain tightly coupled. The momentum-interpolation method, first proposed by Rhie & Chow (1983), has been used successfully in Reynolds-averaged closure calculations, but its performance for turbulence simulations is relatively recent (Zang *et al.* 1994 and Morinishi *et al.* 1998). A drawback of the co-location method is that for inviscid flows strict energy conservation is broken since different discrete divergence operators are used in the continuity equation and the pressure gradient term in the momentum equations. However, the spatial order of this error is less than the discretization error of the basic scheme (Ferziger & Perić 1996, p.188).

The type of spatial differencing dictates the positioning of the contravariant flux velocities relative to the cell-centred Cartesian velocities. In the present DNS code, the spatial differencing is pseudospectral along transformed horizontal coordinates and second-order finite difference in the transformed vertical direction (see §3.1). For this mixed differencing scheme, the natural location of U and V is at cell centres with W positioned at upper and lower cell faces as sketched in figure 2. In a completely finite-difference algorithm all flux velocities are located at cell faces (Zang *et al.* 1994). The particular cell-centred arrangement used here coupled with a conformal grid transformation requires storage for only three metric quantities, (ξ_x, ξ_z, J). This is in contrast to staggered grid methods which need storage for large numbers of metric elements (e.g. Rosenfeld, Kwak & Vinokur 1991).

3.1. *Spatial and temporal discretization*

The flows of interest are assumed to be periodic in (ξ, η)-planes so that spatial derivatives $\partial/\partial\xi$ and $\partial/\partial\eta$ can be evaluated using fast Fourier transforms as in a standard pseudospectral method. All vertical derivatives $\partial/\partial\zeta$ are evaluated using second-order finite differences that account for non-uniform vertical spacing (see §3.3).

The advective terms in the momentum equations are discretized in so-called skew-symmetric form (Arakawa 1966), i.e. $\partial U_j u_i/\partial\xi_j = \frac{1}{2}\left(\partial U_j u_i/\partial\xi_j + U_j \partial u_i/\partial\xi_j\right)$. Zang (1991) performed extensive tests, in turbulent flows, comparing skew-symmetric and rotational forms of the advective terms and concluded that the skew-symmetric formulation is superior even in the presence of aliasing errors. Finally, after each time step flow variables are dealiased in (ξ, η)-planes using the 2/3 rule (Gottlieb & Orszag 1977).

The flow variables are advanced from time step $|^n$ to $|^{n+1}$ using a third-order three-substep Runge–Kutta method (Spalart, Moser & Rogers 1991). All variables are treated explicitly and the pressure is determined as in a fractional step scheme that satisfies the incompressibility condition at the end of each substep. The rule to advance the Cartesian velocity variables at any substep k is

$$u_i|^k = \hat{u}_i|^{k-1} - \Delta t \gamma_k J \frac{\partial}{\partial\xi_j}\left(\frac{p}{J}\frac{\partial\xi_j}{\partial x_i}\right)\Bigg|^{k-1}, \tag{3.1}$$

where the intermediate velocity

$$\hat{u}_i|^{k-1} = u_i|^{k-1} + \Delta t \gamma_k J R_i|^{k-1} + \Delta t \psi_k J \left[R_i - \frac{\partial}{\partial \xi_j} \left(\frac{p}{J} \frac{\partial \xi_j}{\partial x_i} \right) \right] \Big|^{k-2}, \qquad (3.2)$$

is not constrained by continuity. In (3.2), R_i denotes all terms on the right-hand sides of the momentum equations (2.8) except the pressure. The superscript k ($k = 1, 2, 3$) denotes the Runge–Kutta substep such that $u|^{k-1} = u|^n$ for $k = 1$ and $u|^k = u|^{n+1}$ for $k = 3$. The weights associated with the third-order Runge–Kutta method are $\gamma_k = (8/15, 5/12, 3/4)$ and $\psi_k = (0, -17/60, -5/12)$.

The contravariant flux velocities are advanced to the new time level (similarly to their Cartesian counterparts) according to the rule

$$U_i|^k = \hat{U}_i|^{k-1} - \frac{\Delta t \gamma_k}{J} \frac{\partial \xi_j}{\partial x_m} \frac{\partial \xi_i}{\partial x_m} \frac{\partial p}{\partial \xi_j} \Big|^{k-1}, \qquad (3.3)$$

which results from substituting (3.1) into (2.10) and the definition of the intermediate contravariant flux velocities:

$$\hat{U}_i|^{k-1} = \frac{\hat{u}_j|_I^{k-1}}{J} \frac{\partial \xi_i}{\partial x_j}. \qquad (3.4)$$

Expression (3.3) differs from (3.1) in that the pressure term is written in chain-rule form instead of strong conservation form (this is advantageous when the pressure Poisson equation is developed). The crucial step in expression (3.4) is the computation of the intermediate velocity $\hat{u}_i$. We follow Zang *et al.* (1994) and interpolate the intermediate velocity components $\hat{u}_i$ to the same location as U_i using a second-order-accurate method (interpolated variables are indicated by the subscript I). For the mixed pseudospectral finite-difference scheme, interpolation is only needed in the construction of the normal contravariant flux velocity W. Cell-centred U and V are constructed by rotations and scalings of the cell-centred velocity vector u_i. Finally, the time step is computed dynamically using a fixed Courant–Fredrichs–Lewy (CFL) condition.

3.2. *Pressure Poisson equation*

The pressure Poisson equation is developed from the continuity equation (2.7) expressed in terms of the contravariant flux velocities. Application of the divergence operator $\partial/\partial \xi_i$ to (3.3) and restricting our attention to two-dimensional conformal transformations leads to the pressure Poisson equation

$$\frac{\partial^2 p}{\partial \xi \partial \xi} + \frac{1}{J} \frac{\partial^2 p}{\partial \eta \partial \eta} + \frac{\partial^2 p}{\partial \zeta \partial \zeta} = \frac{1}{\Delta t \gamma_k} \frac{\partial \hat{U}_i}{\partial \xi_i}, \qquad (3.5)$$

which applies at each substep k. Notice that except for the variable coefficient that appears in the η-derivatives (3.5) is identical to its counterpart in the case of flat boundaries.

Our pressure solver uses an iterative approach that determines p from

$$\left[\frac{\partial^2 p}{\partial \xi \partial \xi} + \frac{\partial^2 p}{\partial \eta \partial \eta} + \frac{\partial^2 p}{\partial \zeta \partial \zeta} \right]_m = \frac{1}{\Delta t \gamma_k} \frac{\partial \hat{U}_i}{\partial \xi_i} + \left[\frac{\partial^2 p}{\partial \eta \partial \eta} - \frac{1}{J} \frac{\partial^2 p}{\partial \eta \partial \eta} \right]_{m-1}, \qquad (3.6)$$

where m denotes the iteration level. The pressure equation (3.6) at iteration m is solved using standard methods starting from a previous estimate of the pressure at iteration $m-1$ (e.g. Sullivan *et al.* 1996). Equation (3.6) is repeatedly solved until the maximum

difference $|p_m - p_{m-1}|$ satisfies a prescribed convergence criterion. Because of the global nature of our pressure solution procedure (two-dimensional Fourier transforms and tridiagonal matrix inversions), the convergence of (3.6) is independent of the number of grid points used. We found that with $ak = 0.1$, $\partial U_i / \partial \xi_i$ was converged to machine zero after about 10 iterations of the pressure solver. We should mention that the overall computational cost could be reduced by using the numerical scheme described by Le & Moin (1991) which only requires a solution of the Poisson pressure equation at the last Runge–Kutta substep.

The specification and numerical implementation of boundary conditions for the pressure equation mimic those used in our LES algorithm (Sullivan *et al.* 1996). We use periodic boundary conditions in horizontal planes and Dirichlet conditions on the normal component of the contravariant flux velocity W at the boundaries, i.e. specifying W along the upper and lower boundaries at the new time level (see §2.5) is sufficient to determine the pressure.

3.3. *Grid generation*

The physical-space grid is built by specifying the point distribution in (ξ, η, ζ)-space and then inverting the coordinate transformation, i.e. a particular (x, y, z) is found by iterating equation (2.3) at each particular value of the transformed coordinates. Equally spaced distributions of ξ and η are used while in the ζ-direction a stretched grid is employed to resolve the viscous wall layers. Non-uniform ζ spacing with clustering near the vertical boundaries and smooth variation in the domain interior is generated with constant algebraic stretching $K_s = \Delta\zeta_{l+1}/\Delta\zeta_l$. Here the stretching factor K_s, the ratio of the spacing $\Delta\zeta$ between any two adjacent vertical nodes l and $l+1$, is determined by specifying ζ_1 and the total number of vertical points. A typical value for the grid resolution used here (see §5) is $K_s = 1.03$.

4. Laminar Couette flow over a wavy boundary

Prior to attempting turbulent calculations of flow over moving surface waves several validation checks of our simulation code were performed. In order to test the surface-fitted grid capability, we simulated two-dimensional *laminar* Couette flow over a stationary wavy boundary similar to that in figure 1. Benjamin (1959) investigated several variants of this idealized flow theoretically and provides closed form solutions for surface pressure and shear stress under the restrictions of small wave slope, zero phase speed, high *Re*, and linear velocity profiles. These analytic solutions provide a convenient benchmark for testing our code. Our co-located three-dimensional code was used to simulate laminar Couette flow with the caveats that a minimal number of spanwise grid points (6 in our case) were used and no disturbances were introduced into the flow. Since three-dimensional disturbances are never triggered the flow remains two-dimensional at all times. Linear (in ζ) u-velocity profiles were used as initial conditions and the computations were carried out at $Re = U_o \lambda / v = 10^4$ using $24 \times 6 \times 32$ grid points in a computational box of size $(L_x, L_y, L_z)/\lambda = (1, 1, 1)$, which is smaller than that shown in figure 1. The first vertical gridpoint was located at $\zeta^+ = \zeta u_* / v = 0.5$. Computations were carried forward until the solutions reached a steady state.

In figure 3, computational results are compared with linear theory (Benjamin 1959 equations (5.6) and (5.9)) for the surface pressure p and stress τ, normalized by u_*^2, for two different wave slopes $ak = (0.01, 0.2)$. At the smaller wave slope, the computations agree quite well with the analytic results for the grid resolution used.
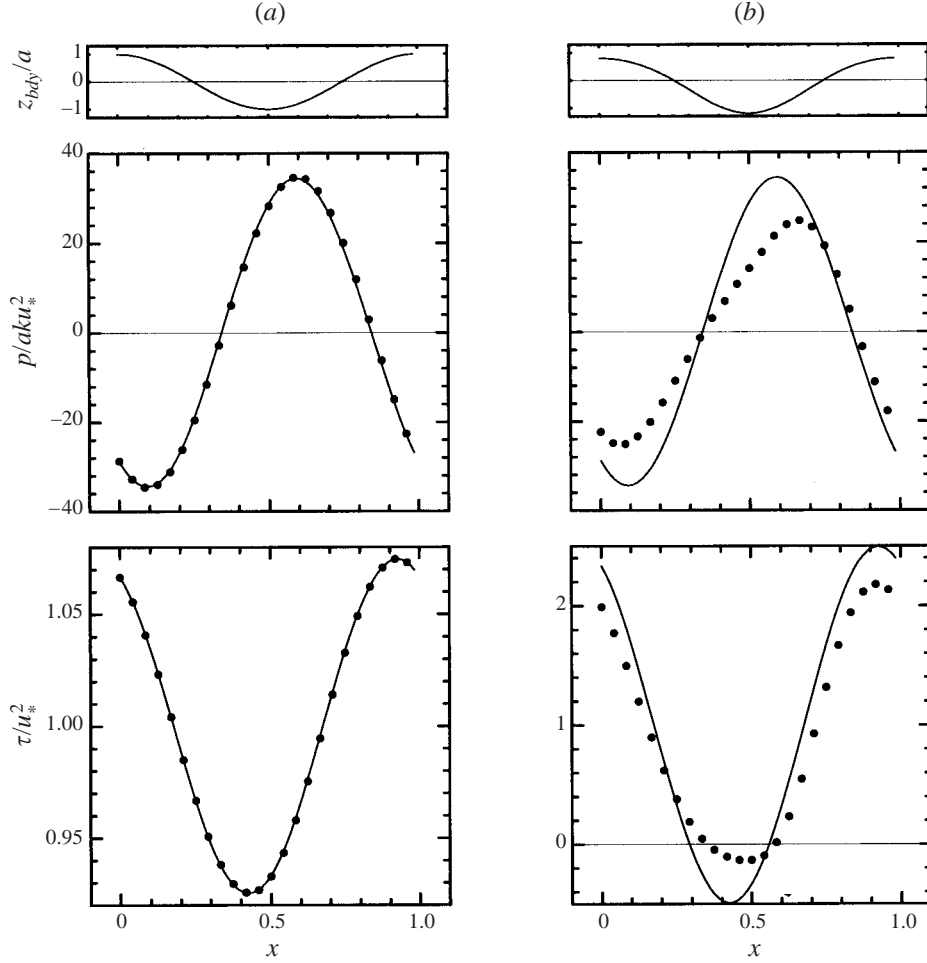
FIGURE 3. Comparison of normalized surface pressure p/aku_*^2 and shear stress τ/u_*^2 from asymptotic theory (Benjamin 1959) (lines) and numerical calculations (dots) for two-dimensional laminar Couette flow at $Re = 10^4$ and $c = 0$. (*a*) wave slope $ak = 0.01$, (*b*) $ak = 0.2$. Normalized wave profile z_{bdy}/a is shown for reference.

The phase location of the peak maximum pressure and minimum shear stress ahead of and behind the wave trough are faithfully captured by the numerics in agreement with the theory. With increasing wave slope the computational solutions gradually depart from the linear theory. At $ak = 0.2$ (where the theory is not expected to be applicable), we see significant deviations from a sinusoidal waveform. The adverse pressure gradient ahead of the wave crest is sufficiently strong to induce a small separated region as evidenced by the negative values of surface stress. Higher wave slopes $ak = 0.3$ (not shown) lead to even larger separated flow regions at this value of Re. In figure 4, the form stress or pressure drag

$$D_p = \frac{1}{\lambda} \int_0^\lambda p \frac{\mathrm{d}z_{bdy}}{\mathrm{d}x} \mathrm{d}x, \qquad (4.1)$$

is plotted as function of the wave slope. Below $ak < 0.1$ the drag estimates from the computations agree quite well with the linear theory, while at $ak > 0.1$ finite wave
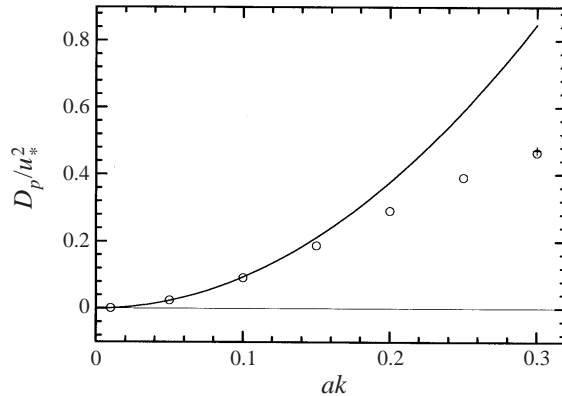
FIGURE 4. Comparison of normalized form stress (drag) between asymptotic theory (line) and numerical calculations (symbols) for two-dimensional laminar Couette flow at $Re = 10^4$ and $c = 0$. ($\circ$, $+$) $24 \times 6 \times 32$ and $48 \times 6 \times 32$ grid points, respectively.

amplitude effects are important and the actual pressure drag falls below the theoretical predictions. A small part of the difference between the theoretical predictions and computations is the departure of the lower boundary (in the computations) from a purely sinusoidal shape with increasing ak (see §2.5). Also shown in this figure is an additional calculation using a resolution of $48 \times 6 \times 32$ gridpoints at the highest wave slope considered. Solutions at $ak = 0.3$ far exceed the regime of validity for the linear theory. Additional grid refinement tests (not presented) that varied the number of gridpoints in both (ξ, ζ) showed that the lowest resolution $24 \times 6 \times 32$ calculations considered produced grid-independent solutions.

5. The turbulent Couette flow experiments

For our turbulence simulations, we consider cases with different values of a and c, including one with a flat, stationary boundary ($a = c = 0$). We choose the Reynolds number sufficiently large ($Re = U_o h / \nu = 8000$) so that the turbulence is fully developed. This Reynolds number is well beyond the transitional value ($Re \approx 2000$) reported by Bech *et al.* (1995). Our Reynolds number is about a factor of 3 higher than the simulations of Komminaho *et al.* (1996) and Bech *et al.* (1995), but 30% less than the simulation of Papavassiliou & Hanratty (1997). The corresponding wall Reynolds number ($Re_* = u_* h / 2\nu$) is about 130.

The number of gridpoints employed is $(N_x, N_y, N_z) = (144, 96, 96)$ which is adequate to capture the dissipation range at our Reynolds number. The vertical spacing $\Delta\zeta$ varies from $0.025/k$ near the surfaces to $0.136/k$ in the middle of the channel (see §3.3); these spacings are equal to 1.0 and 5.5 in wall units, $\Delta\zeta^+ = \Delta\zeta u_*/\nu$.† In the (ξ, η) directions, $\Delta(\xi, \eta) = (0.262, .327)/k$ or $\Delta(\xi^+, \eta^+) = (10.8, 13.5)$. Our computational domain accommodates six waves in the ξ-direction, and thus we have 24 gridpoints per waveform. These grid spacings are comparable to other DNS of turbulent Couette flow over a flat boundary (e.g. Komminaho *et al.* 1996).

The choice of computational domain size, a, λ, and Re represent a compromise between the competing needs to have small a with minimal flow disturbances in the

† Throughout our discussion, velocity and length scales normalized by wall variables, i.e. $(u_*, \nu/u_*)$, are indicated by ( )$^+$.

ak	c	c/u_*	c/u_λ	$u_* \times 10^2$	D_p/u_*^2	κ	z_o^+	$[u_w w_w]/\langle uw \rangle$	$[u_w^2]/\langle u^2 \rangle$
0	0	0	0	3.13	0	0.41	0.17		
0.1	0	0	0	3.21	0.129	0.41	0.22	-0.133	0.016
0.1	0.125	3.91	0.226	3.20	0.181	0.35	0.60	0.072	0.119
0.1	0.25	7.84	0.453	3.19	0.124	0.34	0.71	0.271	0.347
0.1	0.365	11.5	0.652	3.17	0.022	0.39	0.26	0.226	0.332
0.1	0.50	16.2	0.879	3.08	-0.016	0.35	0.39	0.148	0.369
0.1	0.70	22.7	1.232	3.08	-0.035	0.37	0.27	0.047	0.441
0.2	0.25	7.32	0.476	3.42	0.262	0.34	1.47	0.538	0.644

TABLE 1. Simulation properties

upper half of the channel and at the same time large a so that the wave effects are visible at finite Reynolds number. The majority of the computations were conducted with wave slope $ak = 0.1$ (see 1) which is considered an acceptable compromise. We are aware that increasing Re would permit further reductions in wave amplitude but only at the expense of significant computational effort in our DNS.

All simulations were started from a linear profile in ζ for the mean horizontal velocity with zero initial perturbations for the velocity fields. Turbulence was triggered by small random perturbations in a temperature field, which was temporarily added as a gravitational force to the w momentum equation. After 120 time steps, this buoyancy forcing was turned off and each simulation was integrated for more than 15 000 time steps, which is more than 300 large-scale (tU_o/h) or 2400 viscous (tu_*^2/ν) time units. Statistics were obtained by a combination of spatial and temporal averaging beginning at time step 5000 (the method used to generate spatial averages over waves is described in §7.1). Some of the bulk statistics were computed at every time step, but others were obtained from post-processing 100 three-dimensional data volumes which were archived at every 100 time steps.

A summary of the bulk simulation properties is given in 1 which lists the wave slope ak, dimensionless phase speed c, wave age c/u_* and c/u_λ, the non-dimensional friction velocity u_*, form stress D_p/u_*^2, von Kármán constant κ, and dimensionless roughness length z_o^+. The method for estimating the log-law constants (κ, z_o^+) is described in §7.4. The alternative form of wave age c/u_λ uses the mean horizontal velocity at one wavelength above the surface u_λ (see §§7.3 and 7.4). The ratios $[u_w w_w]/\langle uw \rangle$ and $[u_w^2]/\langle u^2 \rangle$ included in table 1 quantify the contribution of the wave-correlated components to the vertical momentum flux and horizontal velocity variance as a function of wave age at a fixed height above the waves, $z = 0.035$ or $kz = 0.22$. This vertical location is approximately twice the wave amplitude from the mean water surface when $ak = 0.1$.

6. Turbulent flow over a flat and stationary lower boundary

An important test of the non-staggered cell-centred algorithm is its ability to simulate turbulent flows since co-located schemes have traditionally only been used for low-Re steady flows. In order to validate the simulation code on a benchmark turbulent flow and at the same time establish a baseline for the effects of surface waves, we consider a flat, stationary lower boundary with all other parameters remaining fixed, thus $(\xi, \eta, \zeta) \equiv (x, y, z)$. This flow then corresponds to classical turbulent Couette flow.
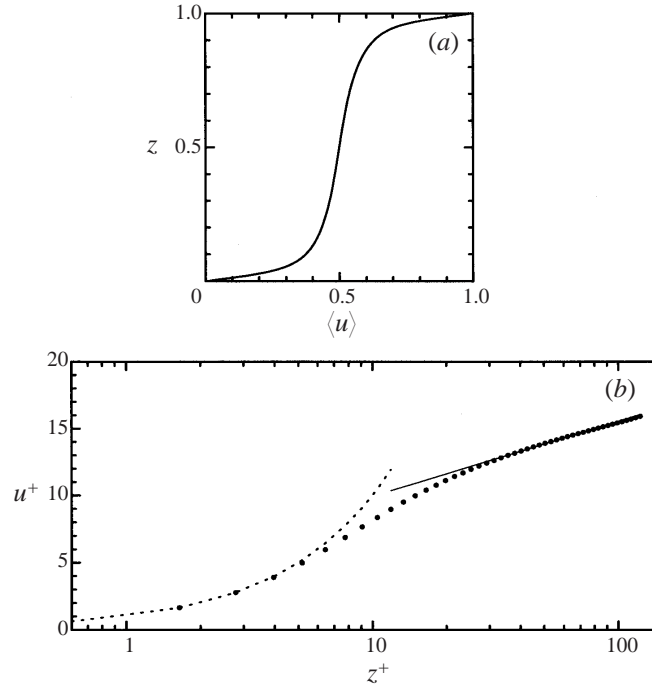
FIGURE 5. Vertical profile of mean horizontal velocity $\langle u \rangle$ for turbulent Couette flow with flat upper and lower walls at $Re = 8000$: (a) non-dimensional global coordinates; (b) wall coordinates where dotted line is $u^+ = z^+$, line is log-law $u^+ = (1/\kappa)\ln z^+ + b$ with $(\kappa, b) = (0.41, 4.3)$, and large dots are computations.

In figure 5, the vertical profile of the mean horizontal velocity component is shown in non-dimensional global coordinates (u, z) and in wall variables (u^+, z^+). As expected the profile is symmetric about the centreline (figure 5a) with sharp gradients near the walls and a more uniform profile in the centre. In wall variables (figure 5b), the variation of the u^+ profile is typical of wall-bounded shear flows; it exhibits a linear region near the wall where $u^+ = z^+$, a buffer (transition) region near $z^+ = 10$, and a log-linear variation $u^+ = (1/\kappa)\ln z^+ + b$ which extends to the channel centreline. We found the log-law constants $(\kappa, b) = (0.41, 4.3)$. Reported values of the log-law constants for turbulent Couette flow over a flat surface, obtained from experiments and other DNS, are in the ranges $0.39 \leqslant \kappa \leqslant 0.43$ and $4.5 \leqslant b \leqslant 6.0$ (Papavassiliou & Hanratty 1997; and Komminaho *et al.* 1996). The experimental data of Aydin & Leutheusser (1991) follow the same trends as our simulation, and also show that the velocity profile at the centre-line becomes more uniform with increasing Re. Overall our mean profiles are consistent with the existing simulations and experimental data.

Under steady conditions, a volume integral of the u momentum equation shows that the total mean vertical stress

$$-\langle uw \rangle + \frac{1}{Re} \frac{\mathrm{d}\langle u \rangle}{\mathrm{d}z} = u_*^2, \tag{6.1}$$

is constant at any z in Couette flow. Figure 6 depicts the turbulent, viscous and total stress components normalized by u_*^2 for the present calculations. Our simulation results closely satisfy condition (6.1) at all z. The turbulent flux $\langle uw \rangle$ is dominant
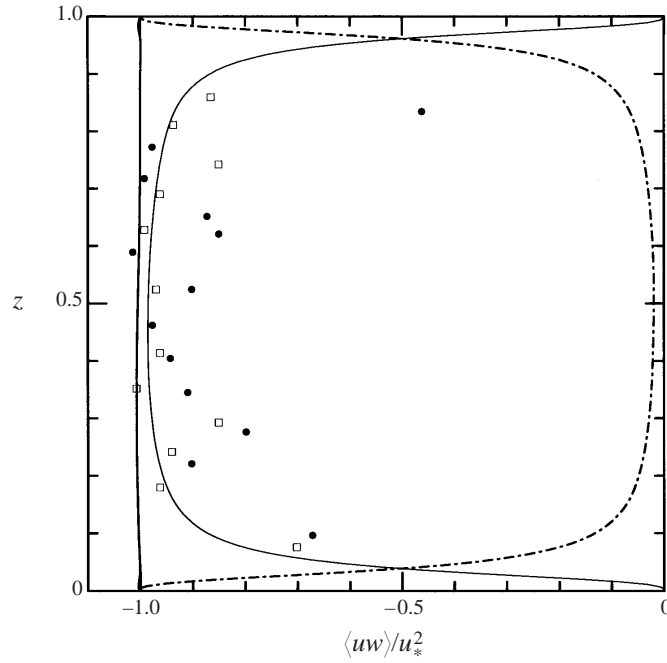
FIGURE 6. Vertical profile of mean vertical turbulent flux $\langle uw \rangle$ (thin line), viscous flux $-(1/Re)\mathrm{d}\langle u \rangle/\mathrm{d}z$ (dash-dotted line), and their sum (thick line) normalized by u_*^2 for Couette flow with flat upper and lower walls, present calculations $Re = 8000$. Data from Aydin & Leutheusser (1991); closed symbols $Re = 5408$, open symbols $Re = 9524$.

over most of the domain with the viscous contribution only significant in a thin region near the boundaries. For comparison, we have included the data of Aydin & Leutheusser (1991) who report measurements of turbulent Reynolds stress, i.e. just $\langle uw \rangle$, for a turbulent Couette flow at Reynolds numbers that are comparable to the present computation. The experimental data, although scattered, show a similar trend to our computation.†

In figure 7, the root-mean-square (r.m.s.) velocity fluctuations for each of the components normalized by the friction velocity $(u, v, w)_{rms}/u_*$ are displayed in global and wall coordinates. The profiles are symmetric about the channel centreline (see figure 7a) as expected. Compared to pressure-driven channel flow the streamwise component at the channel centreline is about a factor of two higher because of the finite mean shear at this position. The streamwise velocity fluctuations attain a maximum $u_{rms}^+ = 2.77$ near $z^+ \approx 15$ in close agreement with other wall-bounded shear flows, e.g. Kim, Moin & Moser (1987) find $(u_{rms}^+, z^+) = (2.7, 15)$. Our computation is in good agreement over the entire domain with the measurements of Aydin & Leutheusser (1991). Note that the DNS of Papavassiliou & Hanratty (1997) are in good agreement with our results despite a difference in the computational box size; their computational domain was $(2\pi, \pi, 1)h$. A smaller domain tends to increase the turbulence variances (Komminaho *et al.* 1996).

---

† Aydin & Leutheusser comment that high turbulence intensity near the wall adversely affects their slanted hot-wire sensors used to measure turbulent flux $\langle uw \rangle$.
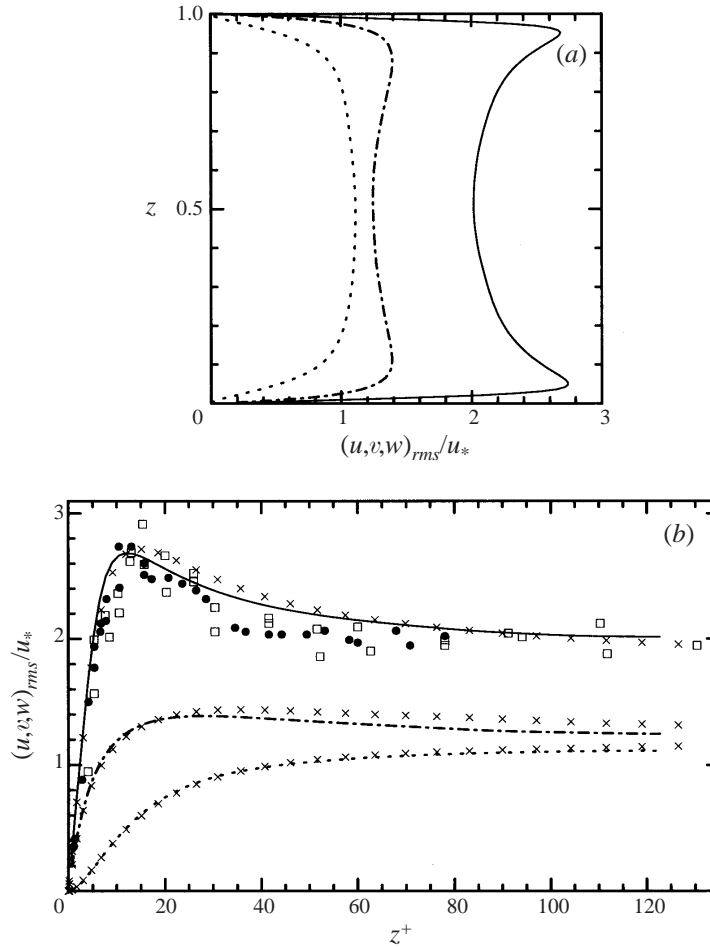
FIGURE 7. Vertical profile of root-mean-square velocity fluctuations normalized by wall friction velocity for Couette flow with flat upper and lower walls at $Re = 8000$: solid line, u_{rms}; dash-dotted line, v_{rms} and dotted line, w_{rms}: (*a*) Non-dimensional global coordinates; (*b*) wall coordinates. Data from Aydin & Leutheusser (1991): closed symbols $Re = 5408$, open symbols $Re = 9524$. DNS results from Papavassiliou & Hanratty (1997): $\times$ symbols $Re = 10640$.

7. Results for turbulent flow over a moving wavy lower boundary

7.1. *Analysis procedures*

In the surface layer of the marine boundary layer, the majority of data sampling, analysis, and interpretation is carried out in a flat Cartesian frame of reference, despite the presence of a geometrically complex lower boundary. Surface layer measurements are usually made well above the tops of the highest waves, and hence no information is obtained about the flow structure very near the air–sea interface. In order to establish a connection with surface layer studies, the analysis and flow visualization in the present work were carried out using both surface-fitted (ξ, η, ζ) and flat Cartesian (x, y, z) coordinates. Each coordinate system has certain advantages and both have been employed in wind–wave laboratory experiments; e.g. Hsu, Hsu & Street (1981) and Hsu & Hsu (1983), use surface-following coordinates while Kendall (1970), and Mastenbroek *et al.* (1996) use a Cartesian frame. Also, results from the recent air–sea

interaction experiments reported by Edson & Fairall (1998) and Hristov *et al.* (1999) were presented in a Cartesian reference frame. Disadvantages of using a Cartesian frame in wind–wave laboratory experiments, as well as in field observations, are the difficulty of positioning probes very close to the interface and the inability to describe the flow near and below wave crests. Despite these drawbacks, the simplicity of using a stationary measuring platform makes fixed probe measurements, and hence Cartesian coordinates, attractive. Accordingly, the flow statistics will depend somewhat on which of the coordinate systems is used.

Simulation results in surface-fitted coordinates were interpolated onto a flat Cartesian grid for analysis using a second-order-accurate method. The Cartesian grid was selected to have the same number of points as the parent surface-fitted grid with uniform spacing in x and y. In the z-direction, a non-uniform point distribution identical to that above a wave crest in the surface-fitted grid was adopted. In the Cartesian frame, the closest approach to the wave form occurs just above wave crests, while the grid lines are slightly more than $2a$ above wave troughs. Thus, we are able to examine the flow characteristics in a Cartesian frame at much closer proximity to the waves than is feasible in wind–wave investigations that use fixed probes.

One of the objectives of this study is to identify wave–turbulence interactions and in particular to isolate motions induced by the presence of surface waves. Thus, both ensemble and so-called 'phase' averages (Hussain & Reynolds 1970) are used to quantify the statistical properties of the flow as well as identify the organized wave components. In a Cartesian frame, an arbitrary random signal f can be defined by (e.g. Hsu *et al.* 1981)

$$f(x, y, z, t) = \langle f \rangle(z) + f_w(x, z) + f'(x, y, z, t), \qquad (7.1)$$

where $\langle f \rangle(z)$, $f_w(x, z)$, and $f'(x, y, z, t)$ are ensemble, wave-correlated, and uncorrelated turbulent components, respectively. The ensemble average $\langle f \rangle(z)$ results from averaging over all (x, y, t). We define a conditional phase average $\overline{f}(x, z)$ as an average over (y, t) and also periodically imaged in x with length λ. Then the wave-correlated component is the difference $f_w(x, z) = \overline{f}(x, z) - \langle f \rangle(z)$. A streamwise average of a wave-correlated component is denoted $[f_w](z)$. The averaging methods discussed above are independent of the choice of coordinate systems and thus we will also present statistics in our surface-fitted coordinates replacing (x, y, z) by (ξ, η, ζ).

7.2. *Flow visualization*

Figure 8 is a visualization of the total fluctuating horizontal velocity (wave-correlated u_w plus turbulent u' components) in a (ξ, η)-plane near the surface for flow over a flat boundary and three cases with moving wavy walls, $c/u_* = (3.9, 7.8, 22.7)$ with $ak = 0.1$. In the absence of waves, the near-surface flow pattern is dominated by streamwise streaky structures which alternate in sign in the spanwise direction, a pattern typical of all flat-wall boundary layers. In the presence of waves, the flat-wall streaky structure is disrupted and the wave forcing leads to small organized pockets of positive and negative fluctuating velocity with horizontal length scales roughly equal to $\lambda/2$. The position of the positive and negative extrema relative to the wave crest depends on c/u_*. For example, the position of maximum $u_w + u'$ for slow moving waves $c/u_* = 3.9$ occurs between the wave crest and trough, while for fast moving waves $c/u_* = 22.7$ the maximum is centred on the wave crest (see § 7.7). The signature of the wave forcing is most apparent for very slow and fast moving waves. In case $c/u_* = 7.8$, the proximity of the critical layer to the lower surface has a significant influence on the flow dynamics (see § 7.6). Flow visualization of the fluctuating u-velocity field (not

shown) reveals large coherent structures at the domain centreline similar to those reported by Komminaho *et al.* (1996) and others. Our visualization indicated that the moving wavy lower boundary did not appreciably alter these long-lived large coherent structures, which form far above the wavy surface.

The importance of waves to the vertical momentum flux is illustrated in figure 9 where a snapshot of the instantaneous flux field $uw = (u_w + u')(w_w + w')$ close to the surface is shown. In the flat boundary case the majority of the turbulent flux is negative and is confined to a few narrow elongated streaky structures. A flux decomposition into quadrants Q1 $(u_w + u', w_w + w' > 0)$, Q2 $(u_w + u' < 0, w_w + w' > 0)$, Q3 $(u_w + u', w_w + w' < 0)$, and Q4 $(u_w + u' > 0, w_w + w' < 0)$, shows that the flux is dominated by Q2 and Q4 motions in the flat case, i.e. by ejections and sweeps. With increasing c/u_* the presence of moving waves clearly alters the flux pattern: both negative and positive pockets appear in the flow visualization. Compared to the flat case, the amplitude of the flux variation with fast moving waves is considerably larger but with a length scale tied to the waves. The quadrant analysis shows a shift in the flux decomposition from Q2 and Q4 (the flat case) to one with more equal contributions from all four quadrants. The appearance of significant Q3 motions coupled with the increase in Q2 is indicative of strong wave forcing that is in quadrature. In an experimental study, Papadimitrakis, Street & Hsu (1988) report that the flux contributions by quadrants are strongly dependent on c/u_* and the location of the critical layer relative to the water surface.

7.3. *Form stress*

One of the crucial differences in flow over waves as compared to flow over a flat surface is the presence of a surface form stress (or drag). Knowledge of the form stress is of importance because it directly influences wave growth (e.g. Belcher & Hunt 1998). Temporal and three-dimensional spatial integration of the u momentum equation (2.8) in surface-fitted coordinates leads to the flux balance

$$-\langle Wu \rangle - \left\langle \frac{p}{J} \zeta_x \right\rangle + \frac{1}{Re} \frac{\partial \langle u \rangle}{\partial \zeta} = u_*^2, \tag{7.2}$$

in the presence of surface waves. Thus, the total flux is conserved along constant-ζ lines, but the viscous and turbulent fluxes are augmented by a pressure flux resulting from the curvature of the ζ-coordinate lines. At the lower boundary $\zeta = 0$, u_*^2 is balanced by both pressure and viscous terms while at $\zeta = 1$ the viscous term equals u_*^2. (Note that by using the identity $\zeta_x/J = -z_\xi$ the pressure term in (7.2) can be shown to be identical to the form stress in equation (4.1) at $\zeta = 0$). In a Cartesian coordinate system, there is no pressure contribution along a level surface and the flux balance at all z above the wave crests is equally described by (6.1).

In order to quantify the magnitude of the pressure contribution, we computed the surface form stress according to equation (4.1) and present the results in figure 10(a) as a function of wave age c/u_* at fixed wave slope $ak = 0.1$. The maximum normalized form stress D_p/u_*^2 is slightly less than 19%. At $ak = 0.2$ the form stress is larger, 30% of u_*^2 (see table 1). The form stress in figure 10(a) is observed to be a strong function of wave age. At small c/u_*, the form stress is positive and acts in concert with the viscous stress to decelerate the flow near the wall, while at large c/u_* an opposite trend is observed: the surface form stress is negative and acts as a thrust in opposition to the surface viscous stress. The critical value of c/u_* that marks this transition occurs at $c/u_*|_{tr} \approx 14$. For comparison, the results from various second-order closure calculations (Li 1995) are also shown in figure 10(a).
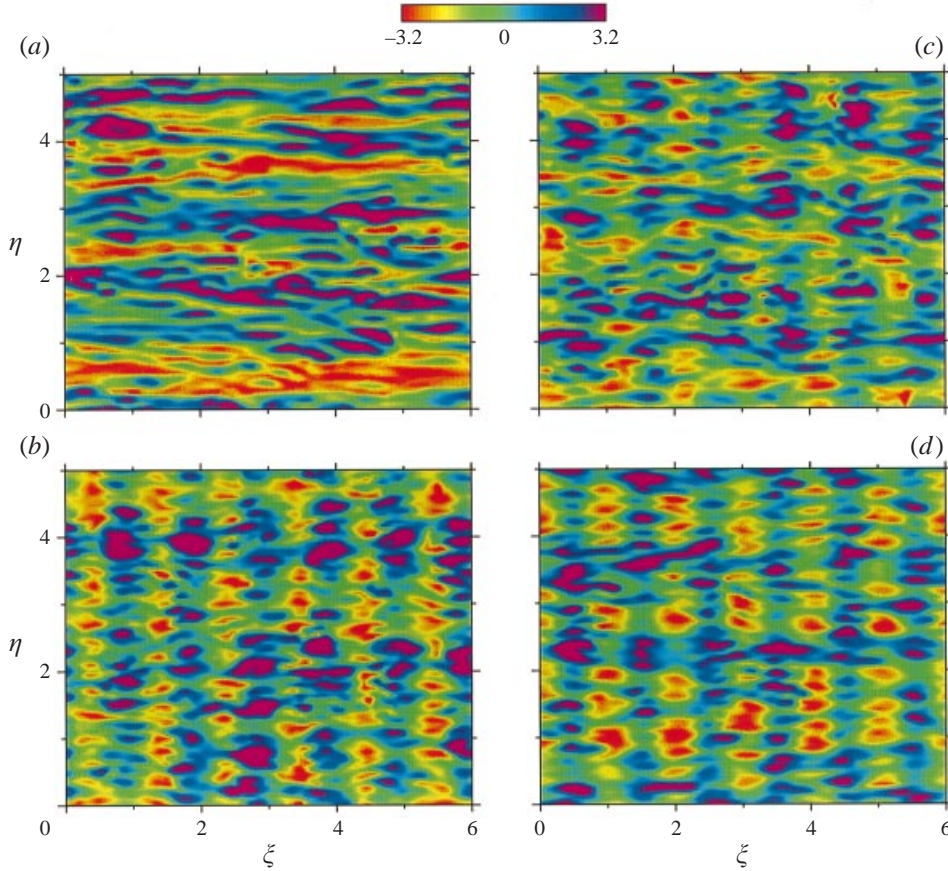
FIGURE 8. Fluctuating velocity $(u_w + u')/u_*$ in a horizontal plane near the lower boundary $\zeta^+ = 5.2$; (*a*) flat case; (*b*) $(c/u_*, ak) = (3.9, 0.1)$; (*c*) (7.8, 0.1); (*d*) (22.7, 0.1).

Our DNS calculations are similar in magnitude, but clearly suggest a $c/u_*|_{tr}$ less than the turbulence closure calculations. This shift is primarily attributable to the different Reynolds number and roughness condition of the lower boundary. The calculations of Li (1995) assume the lower surface is aerodynamically rough and the flow is Reynolds number independent so that the mean velocity profile is presumably logarithmic right down to the water surface. Both Reynolds number and surface roughness influence the form drag (Harris *et al.* 1996 and Gent & Taylor 1976). Field observations (see figure 6 from Gent 1977) also predict a similar sign change of the surface form stress with increasing wave age, although the data for fast moving waves are scattered. Gent & Taylor (1976) and Gent (1977) using a nonlinear model with a turbulence closure also predict a sign change of the form stress with increasing wave age.

The sensitivity of the transition point $c/u_*|_{tr}$ to Reynolds number is not entirely unexpected because of the known dependence of u_* on Re. In an attempt to eliminate this dependence, we consider the drag estimates versus a wave age based on c and a characteristic mean velocity, c/u_λ, shown in figure 10(*b*). Here, u_λ is the mean horizontal velocity at a height of one wavelength above the surface $z = \lambda$ (the wind profiles in §7.4 are used to estimate u_λ). In terms of c/u_λ, the variation of the transition point is much less (0.8 to 0.9), suggesting that the transition point scales with the outer mean velocity over a significant range of Reynolds number. However,
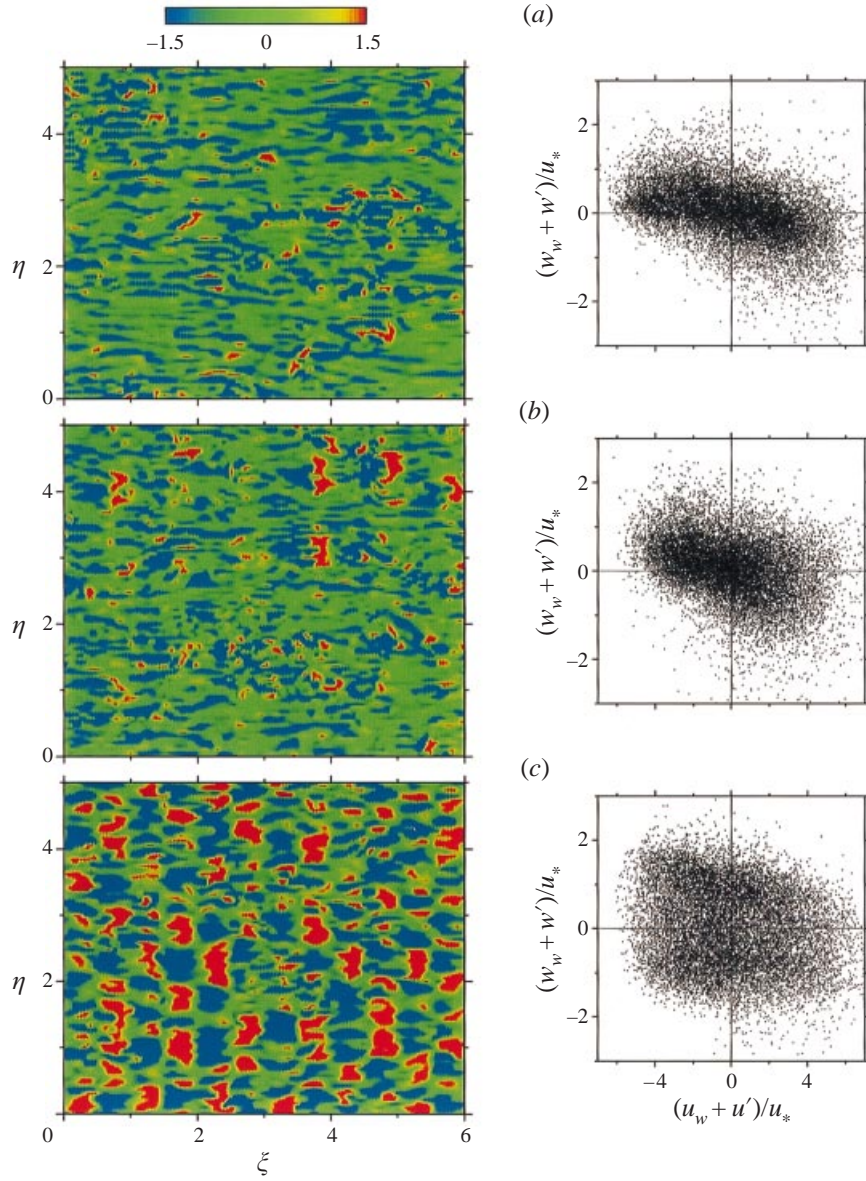
FIGURE 9. Vertical momentum flux $(u_w + u')(w_w + w')/u_*^2$ in a horizontal plane near the lower boundary $\zeta^+ \approx 15$: (a) flat case; (b) $(c/u_*, ak) = (7.8, 0.1)$; and (c) $(c/u_*, ak) = (22.7, 0.1)$. Panels on the right depict the flux decomposition by quadrants.

the magnitude of the maximum form stress still increases with decreasing Reynolds number, a trend also predicted by the asymptotic analysis of Benjamin (1959) and the numerical results of Harris *et al.* (1996).

In the discussion that follows, we categorize the flow by wave age, either as young (slow moving) waves $c/u_* < c/u_*|_{tr}$ (with positive form stress) or old (fast moving) waves $c/u_* > c/u_*|_{tr}$ (with negative form stress). We note that our classification differs from that used by Belcher & Hunt (1998). They classify the flow regime by wave age based on the height of the inner equilibrium layer; they predict slow waves
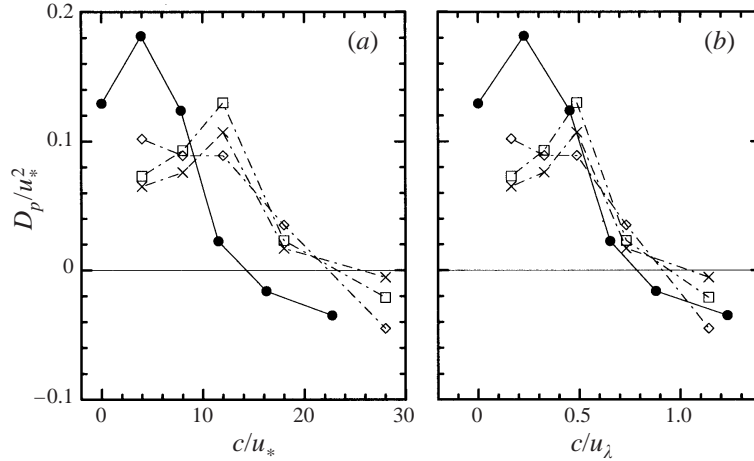
FIGURE 10. Surface form stress normalized by u_*^2 as function of (a) c/u_* and (b) c/u_λ with $ak = 0.1$. Values from our DNS are marked with solid dots, and the open symbols indicate values from three different turbulence closure calculations by Li (1995): $E - \kappa z$ ($\diamond$), $q^2 l$ ($\square$), and Launder–Reece–Rodi ($\times$) turbulence models.

$c/u_* < 15$, intermediate waves $15 < c/u_* < 25$, and fast waves $25 < c/u_*$. However, their quantitative classification based on c/u_* is not directly applicable to the present case since they consider flows with rough walls and infinite Reynolds number.

7.4. *Mean velocity profiles*

The effect of moving water waves on the mean velocity profiles is one of the open questions in air–sea interaction. Does the presence of moving waves modulate the near-surface flow leading to departures from the usual log-law variation over a stationary flat surface? In order to examine this issue, we compared the mean velocity profiles from our simulations to the log-law

$$u^+ = \frac{1}{\kappa} \ln z^+ + b \equiv \frac{1}{\kappa} \ln \frac{z^+}{z_o^+} \equiv \frac{1}{\kappa} \ln \frac{z}{z_o}, \qquad (7.3)$$

which was assumed to apply to all profiles starting at $z^+ > 25$. A least-squares curve fit of the profiles determined κ and b, and hence $z_o^+ = e^{-\kappa b}$ (Yaglom 1979). We estimate the error bar associated with determining κ, b, and z_o^+ to be smaller than 1%.

The variation of the log-law constants in table 1 implies a small but persistent effect on the von Kármán constant: κ is about 10% lower in the presence of moving waves compared to either a flat surface or a stationary wavy surface with $ak = 0.1$. This change is attributed to the wave motion since the variation of Re across all the simulations is quite small, less than 4%. Cases with large positive form stress, i.e. slow moving waves, have slightly lower values of κ than fast moving waves. The value of κ near the transition between positive and negative form stress is only slightly lower than the value obtained over a flat surface.

The effect of waves on the roughness length z_o^+ is however quite pronounced. Given the relatively small variation in κ and the dependence $z_o^+ = e^{-\kappa b}$, our results show that the change in z_o^+ with wave age is dominated by changes in the log-law intercept b. The utility of z_o^+ is its basis for classifying the sea surface condition. For example, Kitaigorodskii & Donelan (1984) summarize a large body of observations over the
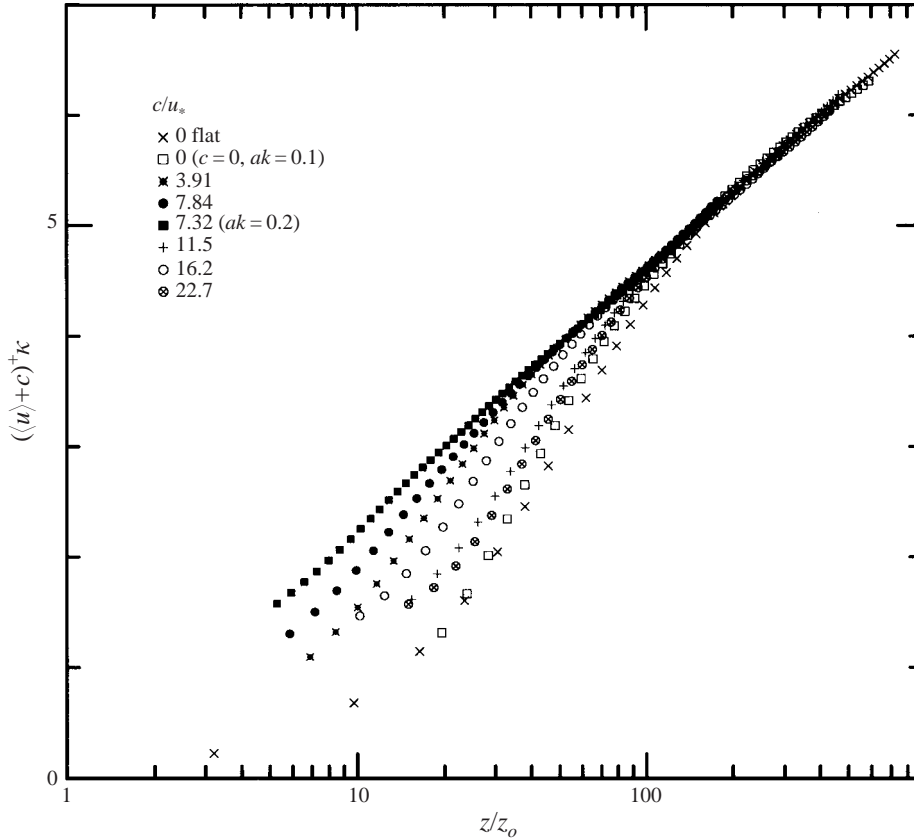
FIGURE 11. Vertical profiles of mean velocity for flow over moving waves of varying c/u_* and ak at $Re_* = 130$. Note that the log-law constants in table 1 are used to collapse the profiles.

ocean and propose the following classification of the sea surface state: $z_o^+ \approx 0.1$ smooth, $0.1 < z_o^+ < 2.2$ transitional, and $z_o^+ > 2.2$ fully rough. The authors further state that the transitional regime is a common sea state. Based on the above criterion, the surface conditions in the present simulations are in the low to middle transitional regime except for case $(c/u_*, ak) = (7.32, 0.2)$ that just approaches the bottom of the fully rough regime. The fact that our predicted z_o^+ lies in the transitional regime suggests that the current low-Reynolds-number DNS simulations are potentially relevant to the geophysical regime.

We found a strong link between roughness length and wave age: slow moving waves are characterized by large z_o^+ while fast moving waves have small z_o^+. This is consistent with the form stress variation in figure 10, where slow moving waves have larger positive drag. With fixed ak, the presence of moving waves can also compound the roughness effect, e.g. z_o^+ is larger for case $(c/u_*, ak) = (7.8, 0.1)$ than for case $(c/u_* = 0.0, 0.1)$. The complicating influences of moving waves is further illustrated if we compare z_o^+ over a smooth flat surface with case $(c/u_*, ak) = (22.8, 0.1)$. Surprisingly, z_o^+ is only slightly greater in the presence of finite-amplitude fast moving waves indicating that the lower surface in this case is nearly as *smooth* as flow over a flat boundary. The speculation that in certain instances moving waves can act as a supersmooth surface was also noted by Hsu & Hsu (1983). Their results were obtained in a wind–wave laboratory experiment at larger Reynolds number and were
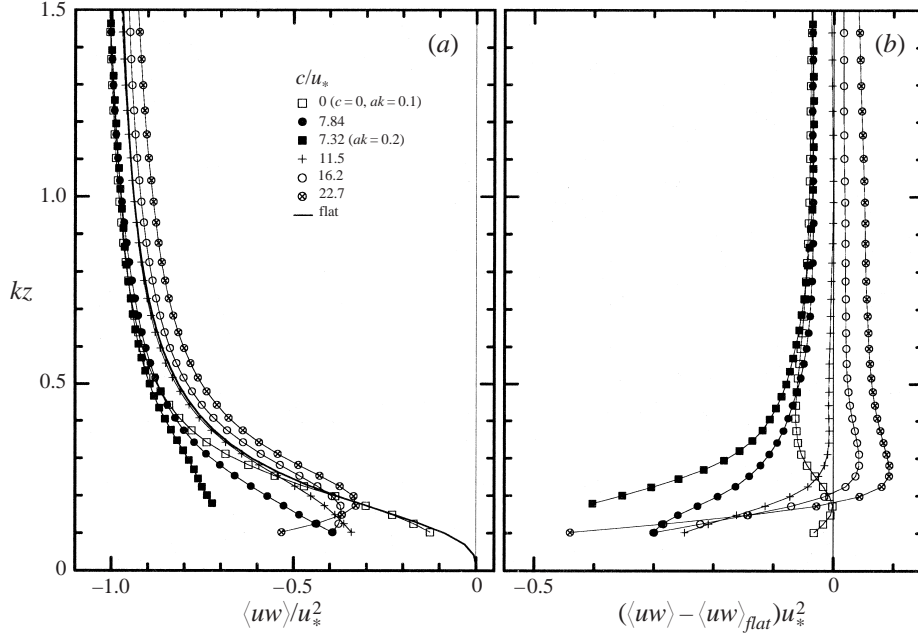
FIGURE 12. Profiles of the average vertical turbulent momentum flux for several values of c/u_* compared to its counterpart over a flat surface: (a) $\langle uw \rangle/u_*^2$, and (b) the vertical momentum flux difference $(\langle uw \rangle - \langle uw \rangle_{flat})/u_*^2$.

attributed to the presence of a surface drift current. In the present DNS, the drift current is set to zero and the change in the effective surface roughness is primarily a result of the sign change of surface form stress and indirectly the location of the critical height as will be discussed later (see §7.6).

In figure 11, vertical profiles of the mean horizontal velocity in log-linear coordinates obtained by analysing the flow in a Cartesian frame (x, y, z) are displayed for varying c/u_*. (Note the dimensionless phase speed is included in the mean profiles, z is measured from the mean water surface, and the constants κ and z_o^+ are taken from 1.) All the profiles collapse to the log-linear variation beyond $z/z_o > 100$. Below $z/z_o < 100$ the profile variation depends on wave age and wave slope. The general trend is that cases with larger z_o^+ display a shorter buffer region and longer logarithmic regions. Notice that for case $(c/u_*, ak) = (7.3, 0.2)$, the velocity profile is near log-linear starting from the crests of the waves, indicative of its approach to the fully rough regime.

7.5. *Turbulence statistics*

Vertical profiles of the mean turbulent momentum flux $\langle uw \rangle$ (i.e. the sum of turbulent and wave-correlated contributions) obtained in the (x, y, z) coordinate system are next shown in figure 12 as function of the non-dimensional distance kz above the mean water surface. The dominant wave effects are confined to the region $kz < 1$ and the variation near the wave surface is complex, depending on both wave age and wave slope. Once again the results can be grouped by wave age c/u_*. This is illustrated in figure 12(b) where the variation of the vertical momentum flux difference, i.e. the momentum flux over waves minus its counterpart over a flat surface at the same kz, is depicted. The momentum flux difference can be as much as 40% of u_*^2 and
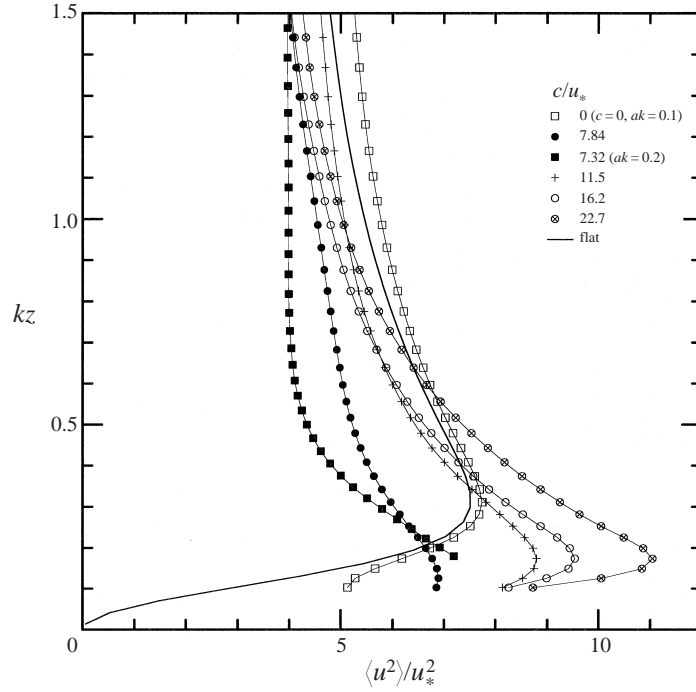
FIGURE 13. Profiles of the average horizontal velocity variance, $\langle u^2 \rangle / u_*^2$, for several values of c/u_*.

hence the presence of a moving wavy surface significantly alters the near-surface turbulent flux. Waves moving slower than $c/u_*|_{tr}$ generate more negative turbulent flux compared to their flat-plate counterparts while fast moving waves display an opposite trend (consistent with the change in form stress). However, very near the surface, the presence of moving waves leads to a more negative average turbulent flux irrespective of c/u_*. These results indicate a complex wave–turbulence interaction near the surface and that the wave-correlated flux is significant (see § 7.7). Evidence for a significant wave contribution is provided in table 1 where the wave-correlated flux can be nearly 30% of the total turbulent flux at $kz = 0.22$ depending on wave age. It should also be noted that the turbulent flux enhancement that occurs near the surface is greater than might be inferred by the form stress; e.g. at $(ak, c/u_*) = (0.1, 7.8)$ the form stress is 12% of u_*^2 while the maximum change in vertical momentum flux is almost 30%. As expected, the variation of the turbulent flux is consistent with the behaviour of the mean velocity profiles as required by equation (6.1).

The influence of moving surface waves is also visible in vertical profiles of the mean turbulence variances $(\langle u^2 \rangle, \langle w^2 \rangle)/u_*^2$, shown in figures 13 and 14, respectively. Similarly to the turbulent momentum fluxes, the results depend on c/u_* and the wave effect is confined to a region $kz < 1$. Compared to the flat case, fast moving waves generate a larger local maximum in the u variance closer to the surface, e.g. at $c/u_* = 22.7$ the maximum $\langle u^2 \rangle/u_*^2 = 11$ occurs at $kz = 0.17$ compared to $\langle u^2 \rangle/u_*^2 = 7.6$ at $kz = 0.3$ for the flat case. The presence of the surface wave orbital velocity, which varies with amplitude akc as described in equation (2.13), is partly responsible for this effect. The wave contribution to the horizontal and vertical velocity variance at a fixed height is especially significant for fast moving waves, as can be seen from
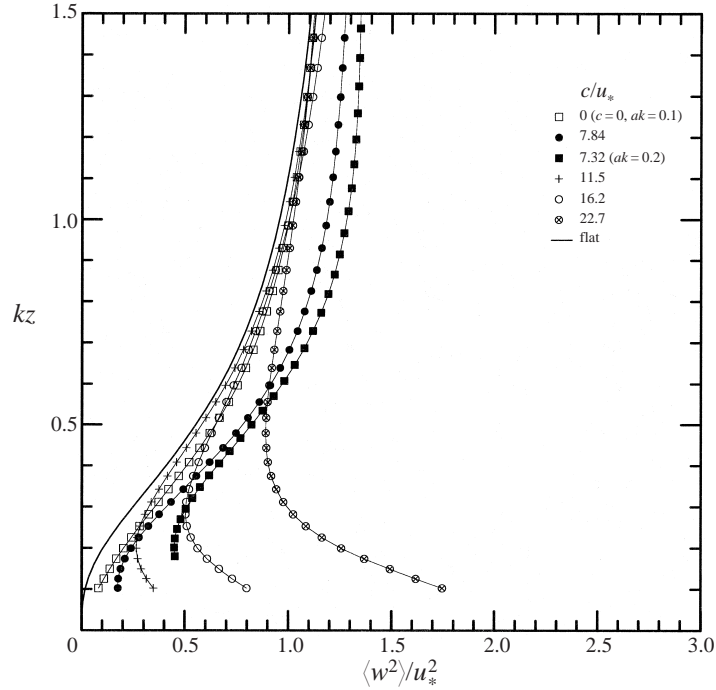
FIGURE 14. Profiles of the average vertical velocity variance, $\langle w^2 \rangle / u_*^2$,
for several values of c/u_*.

table 1 and figure 14. One of the noticeable features in the u variance profile is a pronounced deficit, compared to the flat case, near $kz = 0.4$ for waves moving slower than $c/u_*|_{tr}$. This is in all likelihood linked to critical layer dynamics (see §7.6) since for this case the critical layer is near $kz = 0.4$. We found that the v variance (not shown) is nearly independent of the surface waves at least for the values of wave slope considered. Henn & Sykes (1999), Cherukat *et al.* (1998), and De Angelis *et al.* (1997) observed a significant increase in v fluctuations on the upwind side of a stationary wave. This increase is probably linked to a separation-reattachment process since the wave slopes considered in these studies ($0.157 < ak < 0.628$) were sufficient to induce separation.

The vertical profile of the root-mean-square turbulent pressure $\langle p^2 \rangle^{1/2}/u_*^2$ is depicted in figure 15 (note p is non-dimensional with ρU_o^2). Compared to the flat lower boundary, the presence of a wavy lower surface generates larger pressure fluctuations at all c/u_*. When waves are present, the pressure fluctuations are least when the net form stress is near zero ($c/u_* \approx c/u_*|_{tr}$) and greatest for fast moving waves. The increased pressure fluctuations for fast moving waves are in part due to the surface orbital velocities which are significant at $c/u_* = 22.7$. The wall limiting value in the case of a flat surface is about 2.5, which is about 60% higher than the value obtained from the DNS by Kim *et al.* (1987) in a pressure-driven channel flow. As noted by Kim *et al.* (1987) the wall-pressure fluctuations show a decreasing trend with Reynolds number, and thus our result tends to support the speculation of Komminaho *et al.* (1996) that the near-wall behaviour of plane turbulent Couette flow is representative of a much higher Reynolds number channel flow.
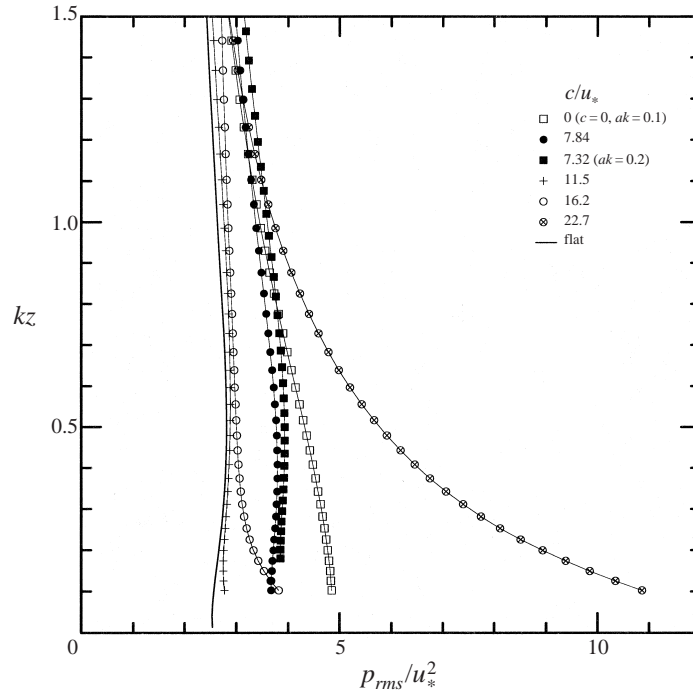
FIGURE 15. Profiles of the root-mean-square pressure, $\langle p^2 \rangle^{1/2}/u_*^2$, for several values of c/u_*.

7.6. *Phase-averaged streamlines and structure of the critical layer*

One of the important aspects of this work is the eduction of flow patterns in the vicinity of a moving wavy surface. In order to isolate the mean wave-induced flow fields, the ensemble- and phase-averaging operators, described in §7.1, were applied to the u and w velocity components in surface-following coordinates. The resulting velocity field consists of ensemble means ($\langle u \rangle, \langle w \rangle$), which are functions of ζ, and wave-correlated components (u_w, w_w), which vary with both (ξ, ζ).

The phase-averaged vectors ($\langle u \rangle + u_w, \langle w \rangle + w_w$) are shown as streamlines in figure 16 for several different values of c/u_* including the reference case $c/u_* = 0$. For a stationary wave, the flow pattern near the surface tends to follow the waveform quite closely. The near-surface winds accelerate on the windward side of the wave because of a favourable pressure gradient, then reach a maximum speed in the vicinity of the wave crest, and finally decelerate on the leeward side of the wave under the action of an adverse pressure gradient. At heights $z > 0.5/k$ the wave effects are small and the mean flow pattern tends to a horizontally uniform mean flow. For the modest wave slope considered, $ak = 0.1$, the flow remains attached and there are no separation points along the wave.

The streamline patterns over moving waves differ from their stationary counterparts in dynamically important ways. Viewed in the wave frame of reference, the average flow near the surface must be opposite in direction to the primary flow aloft for non-zero c/u_* as required by the surface boundary conditions (see §2.5). A measure of the vertical extent of the reversed flow region is the height of the critical layer z_{cr} (e.g. Belcher & Hunt 1998). The critical layer height z_{cr}, shown as the dotted line in figure 16, is defined as the vertical location where the total streamwise velocity is identical to zero, i.e. where $\langle u \rangle + u_w = 0$. At low c/u_*, z_{cr} is small, $z_{cr} < 0.1/k$, and
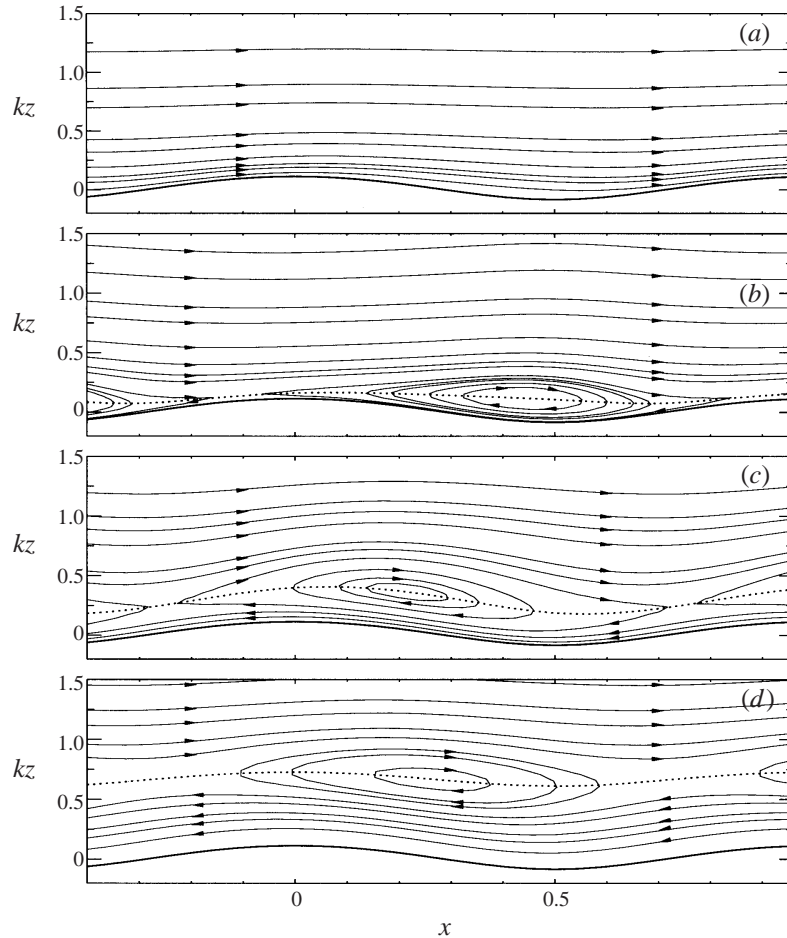
FIGURE 16. Phase-averaged streamlines over stationary and moving waves with $ak = 0.1$ in sur-face-fitted coordinates: (*a*) $c/u_* = 0$; (*b*) $c/u_* = 3.9$; (*c*) $c/u_* = 7.8$; (*d*) $c/u_* = 11.5$. The dotted line corresponds to the height of the critical layer where $\langle u \rangle + u_w = 0$.

is strongly asymmetrical about x, being thinner on the windward side of the wave and thicker on the leeward side. At moderate $c/u_* = 7.8$, z_{cr} is higher, tends to follow the wave shape and there is less asymmetry compared to the case with lower c/u_*. Finally, for fast moving waves $z_{cr} > 0.5/k$ and is nearly flat, independent of x.

The structure and importance of the critical layer in flow over moving waves has been the subject of much analysis. Critical layer phenomenon is the central ingredient in Miles' (1957) inviscid analysis and the physical interpretation of wave growth presented by Lighthill (1962). A consequence of the critical layer is that a region of closed streamlines or 'cat's-eyes' must occur if there is any periodic variation of the mean flow along the wave, e.g. Lighthill sketches a symmetrical cat's-eye pattern directly over the wave crest. However, the linearized theory of Townsend (1972) termed the critical layer merely an unimportant part of an equilibrium layer if turbulence is considered. Also, Mastenbroek (1996) pointed out that none of the numerical studies of turbulent flow using second-order closure over slowly growing waves demonstrated any dynamical effects of a critical layer. It should be noted that second-order closure

has shown the importance of the critical layer in other flow regimes, e.g. in gravity wave turbulence interaction (Einaudi, Finnigan & Fua 1984).

Figure 16 readily shows that a cat's-eye pattern exists in our simulations and is centred about the critical layer height. There are no separation or re-attachment points at the surface (the cat's-eye pattern does not extend to the surface) and hence the flow over moving waves at this wave slope is attached at least for the mean flow (e.g. Gent & Taylor 1977). However, turbulent fluctuations could potentially lead to transient small separated zones.

At low c/u_*, the mean cat's-eye hugs the lower boundary with its centre located just upwind of the wave trough ($x \approx 0.4$) and extends nearly over the entire wavelength. Directly above the centre of the cat's-eye pattern the flow is displaced vertically and no longer follows the wavy lower boundary. In other words, the region of closed streamlines, which encompasses relatively slow moving fluid, acts similarly to an obstacle to the fast moving flow above z_{cr} (i.e. the outer flow) deflecting the outer mean streamlines away from the moving wavy surface. Thus, the critical layer is dynamically important as it alters the mean flow patterns above the waves, disrupting the tendency to follow the lower boundary. With increasing wave celerity, the centre of the cat's-eye pattern moves closer to the crest ($x \approx 0.2$) and is displaced to an even greater extent vertically. The vertical displacement is necessary to accommodate the greater flow beneath the cat's-eye with increasing wave speed. The overall horizontal extent of the cat's-eye pattern appears to be a maximum for $c/u_* = 7.8$, as is the disruption of the outer mean streamlines. At $c/u_* = 11.5$, the centre of the cat's-eye pattern is lifted well off the surface and only slightly perturbs the near-surface pattern. The size, shape, and streamwise and vertical locations of the mean cat's-eye pattern, from our DNS, are clearly dependent on c/u_*, but overall are centred between the crest and trough and are at least as thick as the wave amplitude a in good agreement with the measurements of Hsu *et al.* (1981).

7.7. *Wave-correlated velocity and momentum flux fields*

The effect of the critical layer on the non-dimensional wave-correlated fields $(u_w, w_w)/u_*$ and their fluxes $u_w w_w/u_*^2$ is next illustrated in figures 17, 18, 19, and 20, which correspond to $c/u_* = (0, 3.9, 7.8, 22.7)$ at fixed $ak = 0.1$. In each figure, we show spatial (x, z) contours of $(u_w, w_w, u_w w_w)$ and vertical profiles of streamwise-integrated wave-correlated fields, i.e. $[|u_w|]$, $[|w_w|]$, $[u_w w_w]$, where $|u_w|$ and $|w_w|$ are absolute values. The contours and shading schemes are not constant across c/u_* but instead are chosen to highlight extrema in the fields for each case. Also, in figures 18 and 19 the critical layer height z_{cr} is shown for reference; z_{cr} does not appear in figure 20 since $z_{cr} > 2/k$ for this value of c/u_*, while z_{cr} coincides with the wavy surface in figure 17 since $c = 0$.

If we consider the reference case $c/u_* = 0$, the positive (negative) extrema in u_w and w_w both occur upwind (downwind) of the crest resulting in a positive wave-correlated flux $u_w w_w$; u_w, w_w and $u_w w_w$ all reach maximum values near $z \approx 0.125/k$. Near the surface, there are small phase shifts between u_w and w_w resulting in pockets of negative flux centred just slightly downwind of the crest and trough. Furthermore u_w and w_w become decorrelated with vertical distance from the boundary because of the gradual downwind tilting of the u_w-contours. At $kz = 1$, the centroid of the u_w-field is almost directly above the wave crest while the centroid of w_w remains almost vertically constant. The vertical profile of the spatially integrated flux $[u_w w_w]$ is zero at the surface because of no-slip boundary conditions, reaches a positive maximum
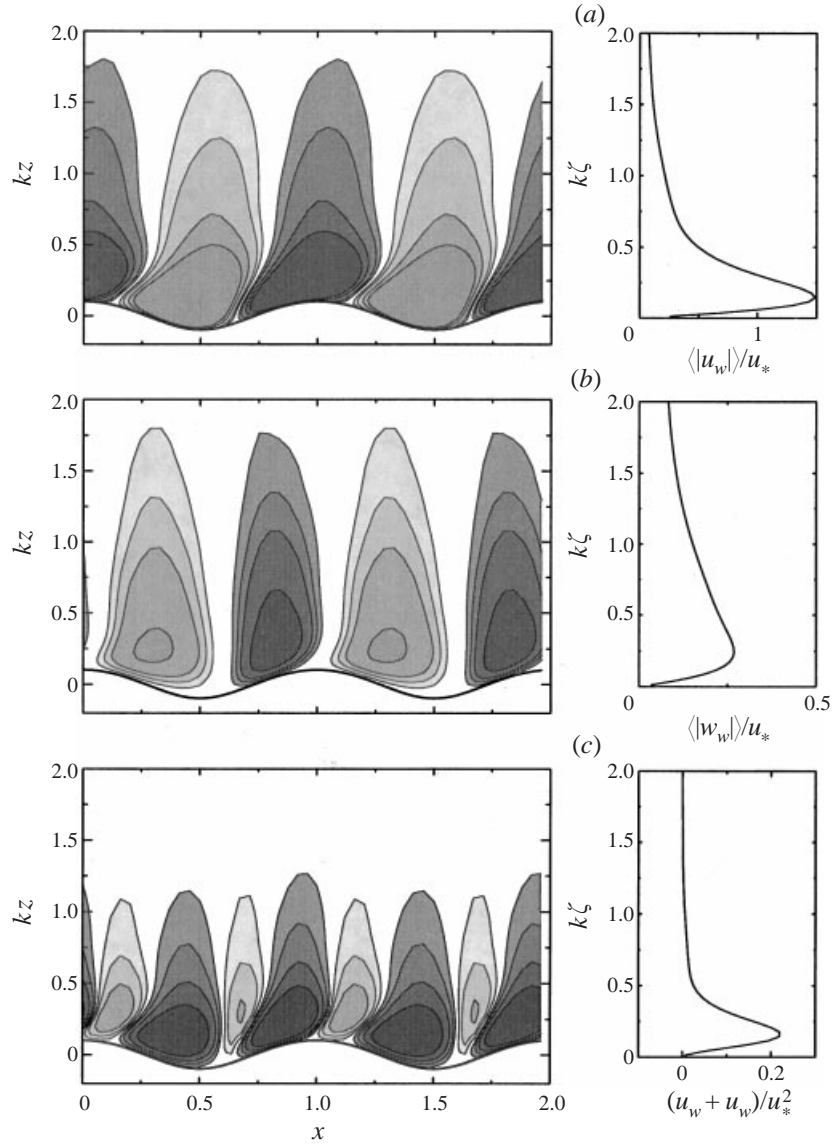
FIGURE 17. Normalized wave-correlated fields $(u_w, w_w)/u_*, u_w w_w/u_*^2$ for case $(c/u_*, ak) = (0.0, 0.1)$ in surface-following coordinates; all contours progress from darker to lighter shading with negative (positive) values for the light (dark) shaded family: (a) u_w, contours $(\pm 0.6, \pm 0.4, \pm 0.2, \pm 0.1)$, magnitude of wave integrated u_w is shown on the right; (b) w_w, with contour values $(\pm 0.1, \pm 0.15, \pm 0.2, \pm 0.3)$; (c) flux $u_w w_w$, contour values $(\pm 0.02, \pm 0.05, \pm 0.1, \pm 0.2)$.

slightly above the surface because of the speedup and slowdown over the wave, and then decays smoothly to zero aloft ($kz > 1$).

For moving waves, $c/u_* = 3.9, 7.8, 22.7$ (figures 18, 19, and 20), the wave-correlated fields exhibit significant departures from the stationary case because of the critical layer and, to a lesser extent, the surface orbital velocities. For $z < z_{cr}$, the effects of the reverse mean flow and the orbital velocity of the water, which varies like $akc \sin kx$, act in concert to produce positive (negative) w_w on the leeward (windward)
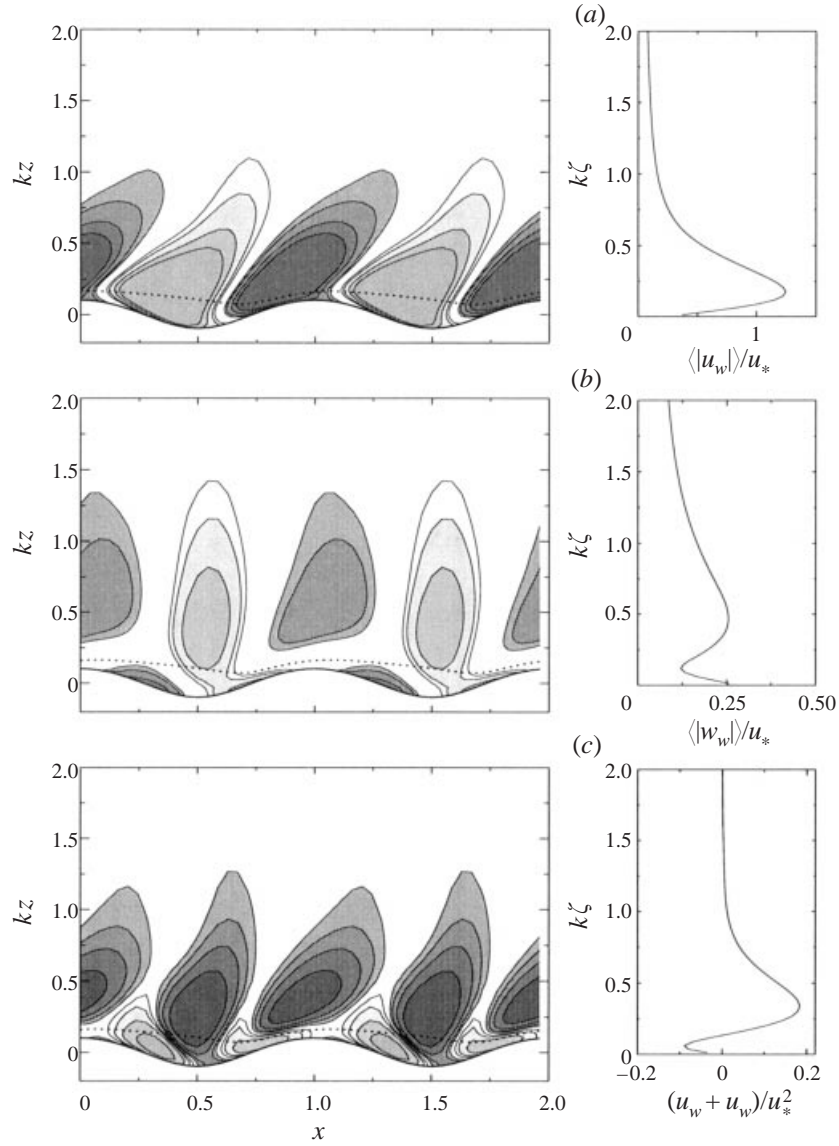
FIGURE 18. As figure 17 but for case $(c/u_*, ak) = (3.9, 0.1)$: (a) u_w, contour values $(\pm 0.2, \pm 0.3, \pm 0.5, \pm 0.7)$; (b) w_w, with contour values $(\pm 0.15, \pm 0.2, \pm 0.3, \pm 0.5)$; (c) flux $u_w w_w$, contour values $(\pm 0.02, \pm 0.05, \pm 0.1, \pm 0.2)$. The dotted line is the critical layer height where $\langle u \rangle + u_w = 0$.

side of the wave, a trend opposite to that in the stationary case. The importance of the water orbital velocity can be seen in the vertical profile of $[|w_w|]$ which becomes dominant near the surface with increasing wave celerity, e.g. $w_w/u_* \sim akc/u_* \approx 2.28$ at $(c/u_*, ak) = (22.7, 0.1)$. For non-zero c/u_*, the horizontal position of the positive and negative extrema in the near-surface w_w remains relatively fixed at $x = \pm 1/4$ from the crest, i.e. where the magnitude of the orbital velocity is maximum. With increasing distance above the surface the wave-correlated w_w decays, and depending on the shape and proximity of the critical layer to the surface, passes through zero at z_{cr} and then changes sign.
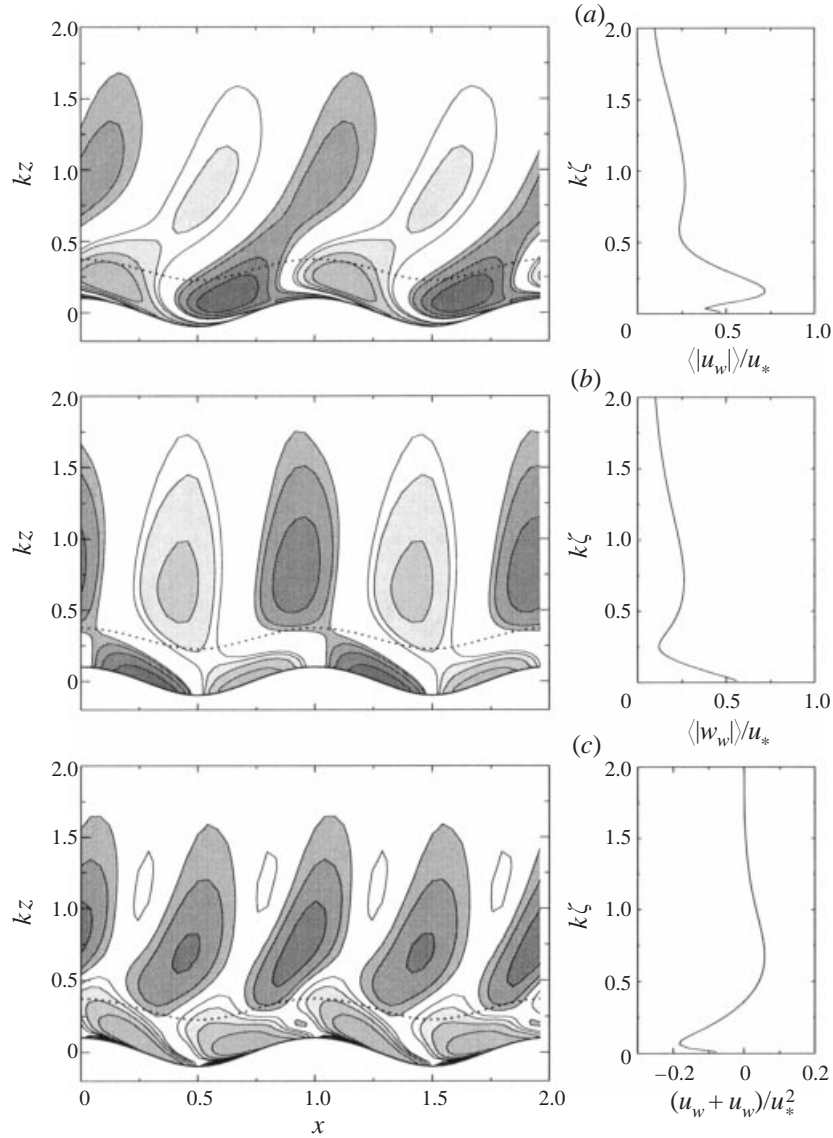
FIGURE 19. As figure 18 but for case $(c/u_*, ak) = (7.8, 0.1)$.

Above the critical layer the (x, z) positions of the maximum and minimum w_w are correlated with the variation of the critical layer: the maximum and minimum in w_w occur upwind and downwind of the peak in z_{cr}, like a stationary surface. However, the vertical oscillation of the critical level is small compared to the undulations of the water surface (i.e. the vertical variation of z_{cr} with x is less than that of z_{bdy}) and hence the magnitude of w_w generated by the cat's-eye patterns above the critical level is smaller than that below z_{cr} at all c/u_*. For fast moving waves ($c/u_* = 22.7$), the critical level is far above the water surface $z_{cr} \gg 2/k$, the orbital velocity of the water is large, and then w_w varies smoothly from $z = z_{bdy}$ up to $z = 2/k$.

Examination of the streamwise wave-correlated contours suggests that the variation of u_w is more complex than w_w, being more tightly coupled to conditions above and
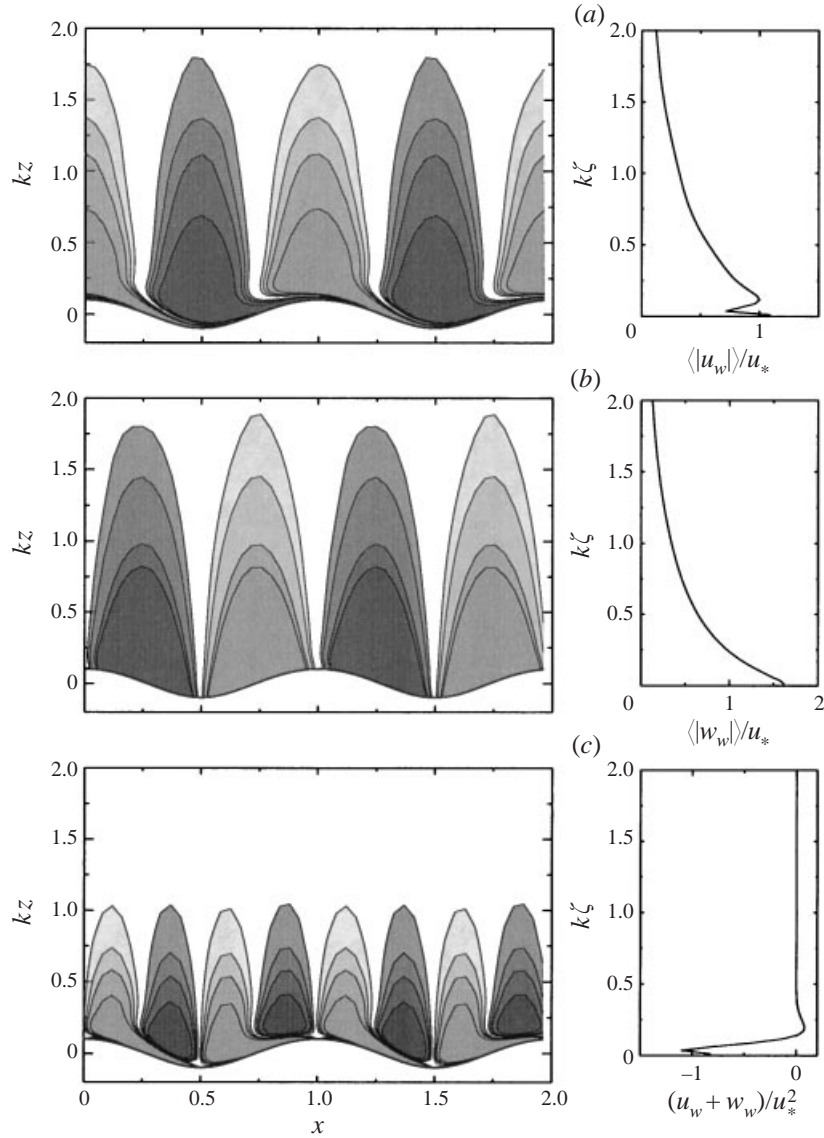
FIGURE 20. As figure 17 but for case $(c/u_*, ak) = (22.7, 0.1)$: (*a*) u_w, contours $(\pm 0.2, \pm 0.3, \pm 0.4, \pm 0.6)$; (*b*) w_w, with contour values $(\pm 0.2, \pm 0.3, \pm 0.5, \pm 0.6)$; (*c*) flux $u_w w_w$, contour values $(\pm 0.1, \pm 0.2, \pm 0.3, \pm 0.5)$.

below the critical height. The pattern of positive and negative u_w contours near the surface shifts to the left (upstream) with increasing c/u_*. At the same time, the contours are displaced vertically because of the surface orbital velocities. The magnitude of the orbital velocity for u is maximum at the wave crest and trough since it varies as $akc \cos kx$ and thus u must change sign in a very thin boundary layer near the surface with increasing c/u_* (see also Hsu & Hsu 1983). This leads to the kink in the vertical profiles of $[|u_w|]$ very near the surface, $z \ll 0.1/k$.

At all c/u_*, $[|u_w|]$ exhibits a maximum near the surface nearly independent of the vertical position of the critical level. Also, u_w varies more smoothly across z_{cr} than
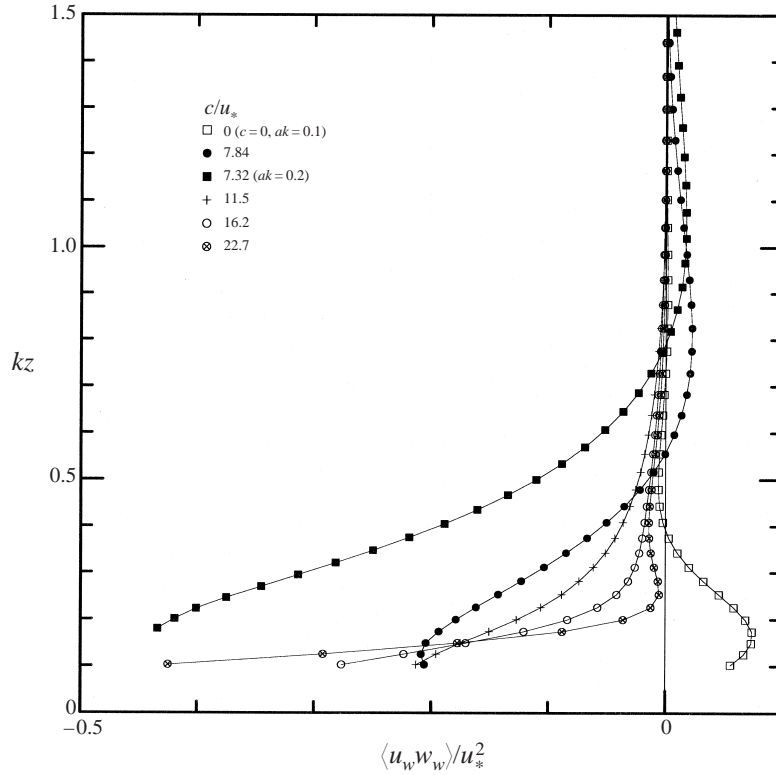
FIGURE 21. Profiles of the wave-correlated vertical momentum flux $\langle u_w w_w \rangle / u_*^2$ above the wavy boundary, for several values of c/u_*.

does w_w. For instance at $c/u_* = 7.8$, where the effects of the critical layer are large, the contours of u_w are continuous across z_{cr} but exhibit a pronounced downwind tilt. The contours of u_w as well as its streamwise integrated value $[|u_w|]$ hint at a minimum near $kz = 0.5$, which is just above the cat's-eye pattern (see figure 16). Above z_{cr}, the streamwise wave-correlated u_w maintains the same sign sense as in the stationary case, but with an exaggerated streamwise bias. This adds further support to the speculation that the critical layer and the formation of a cat's-eye pattern alters the effective shape of the lower boundary that the outer flow sees, i.e. the flow above the critical layer responds to the geometry given by z_{cr}. Overall, our results are in agreement with the speculation of Belcher & Hunt (1998) who suggest that for intermediate wave speeds the reversed flow beneath the critical layer would generate an asymmetric flow upwind of the crest while above z_{cr} the asymmetry would be downwind.

The wave-correlated flux $u_w w_w$ further reflects the importance of the critical layer. Beneath z_{cr}, $u_w w_w$ is predominantly negative (and hence so is $[u_w w_w]$) and decreases (becomes more negative) with increasing c/u_*. For intermediate c/u_*, where the effects of the critical layer are important $u_w w_w > 0$ for $z > z_{cr}$ similarly to flow over stationary waves. The magnitude of $u_w w_w$ in the outer region is however small because of the progressive tilting of the wave-correlated streamwise velocity. Our results for $u_w w_w$ are similar to the measurements of Hsu *et al.* (1981) who show that the wave-correlated flux is positive (negative) above (below) the critical layer. Kendall (1970) and Takeuchi, Leavitt & Chao (1977) were not able to obtain measurements very
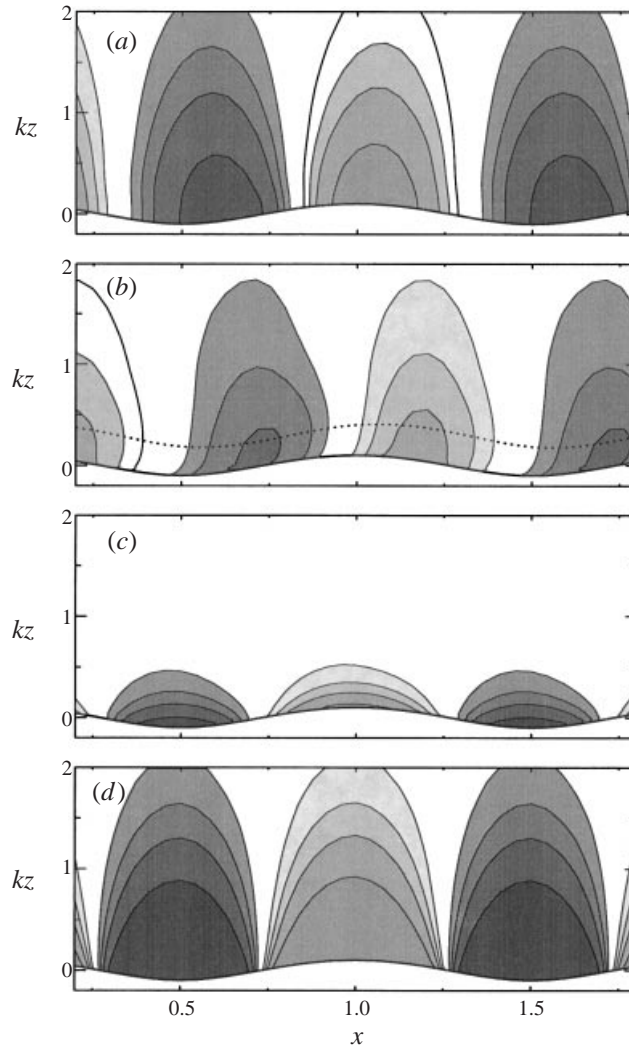
FIGURE 22. Normalized wave-correlated pressure p_w/u_*^2 in surface-following coordinates for flow over surface waves with $ak = 0.1$; contours progress from darker to lighter shading with negative values $(-4.0, -2.4, -1.6, -0.90)$ for the light shaded family and complementary positive values for the dark shaded family; (a), (b), (c), (d) correspond to $c/u_* = (0, 7.8, 16.2, 22.7)$. The critical layer height is denoted by a dotted line.

near the surface, but in the outer region their results indicate that $u_w w_w$ is positive for slow moving waves and becomes negative as c/u_* increases similar to the present DNS.

Finally, in figure 21 we show profiles of the normalized integrated wave-correlated flux obtained by analysing the data in flat coordinates, $[u_w w_w]/u_*^2$. The important aspect to observe here is that the trends noted previously in surface-following coordinates also persist when the data are analysed in flat coordinates. Thus, we conclude that the variation of $u_w w_w$ with c/u_*, and in particular the influence of the critical level, is not an artifact of the analysis procedure and might be identified with measurements made near the water surface (e.g. Hristov *et al.* 1999). Also, note that
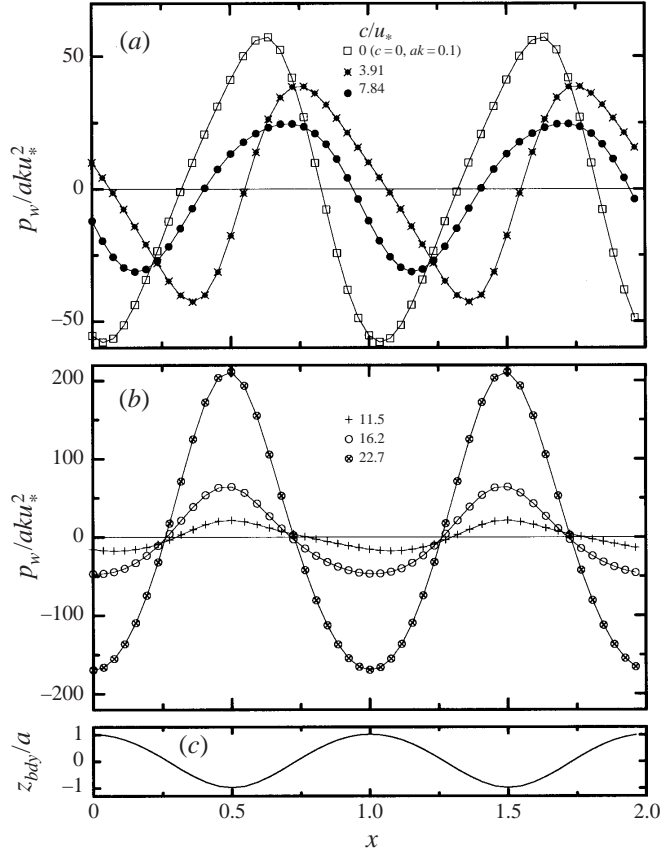
FIGURE 23. (a, b) Normalized wave-correlated surface pressure p_w/aku_*^2 for flow over surface waves with $ak = 0.1$ and varying $c/u_* = 0, 3.9, 7.8, 11.5, 16.2, 22.7$. The normalized wave shape z_{bdy}/a is shown in (c).

at $(c/u_*, ak) = (7.32, 0.2)$ the wave-correlated flux in the vicinity of the waves is a substantial contributor to the total flux, more than 40% of u_*^2.

7.8. *Wave-correlated pressure and surface stress fields*

The effects of surface waves on the pressure field are illustrated in figures 22 and 23 for several values of c/u_*. Compared to the wave-correlated velocity field, the wave-correlated pressure signal can extend to much higher elevations above the waves. Also, the contours reach vertically in a smooth manner for all cases shown except for $c/u_* = 7.8$, i.e. where the critical layer has the greatest impact on the velocity field. In the $c/u_* = 7.8$ case, the pressure field contours show a pronounced tilt in the downstream direction below z_{cr} whereas above z_{cr} the contours bend back upstream. With increasing c/u_*, the region of minimum pressure first moves downstream towards the trough but eventually retreats back upstream. At the highest c/u_*, the minimum (maximum) pressure is nearly centred over the wave crest (trough), which results in a small negative form stress (see figure 10). If we examine the variation of the r.m.s. pressure in figure 15, we observe that the wave-correlated pressure component can more than double the pressure fluctuations depending on c/u_*. The largest r.m.s. pressure is observed for fast moving waves which is also the case with the largest wave-correlated pressure component. Similarly the case with the smallest
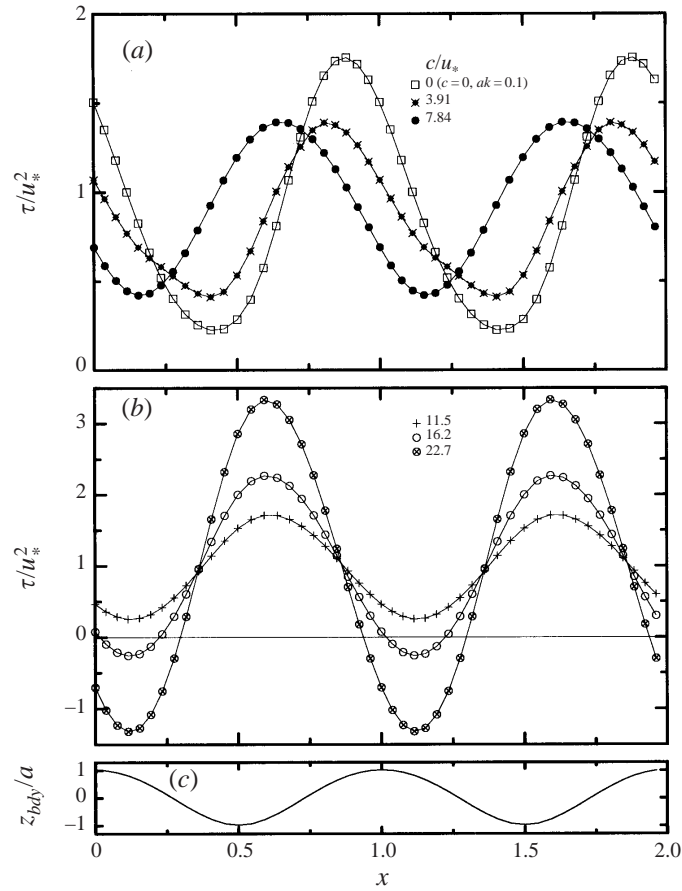
FIGURE 24. Normalized wave-correlated surface stress τ/u_*^2 for same conditions as in figure 23.

wave-correlated pressure, $c/u_* = 16.2$, has the lowest r.m.s. pressure fluctuations. It should also be noted that the strength of the wave-correlated pressure component in case $c/u_* = (3.9, 7.8)$ is noticeably smaller than either a stationary wave $c/u_* = 0$ or fast moving waves $c/u_* > 16$. However, case $c/u_* = (3.9, 7.8)$ has higher form stress (see figure 10) because of the optimal location of the pressure field on the wave itself, i.e. the streamwise location of the pressure field has a higher correlation with dz_{bdy}/dx and thereby generates a larger positive surface drag. The surface pressure deviates from an ideal sinusoidal waveform suggesting that nonlinearities and turbulence are important at a modest wave slope, $ak = 0.1$ for all c/u_*.

The variation of the wave-correlated viscous stress parallel to the wave surface (shown in figure 24) also depends strongly on wave age. With increasing wave age, the maximum value of τ/u_*^2 gradually shifts from near the crest to a location nearer the trough. This movement of the stress maximum coincides with the spatial shift in the wave-correlated velocity maximum $\langle|u_w|\rangle$ (see part (a) of figures 17–20). With increasing wave age, the absolute value of the maximum and minimum surface stress both increase. At the same time, the effect of the imposed surface orbital velocities is visible. For instance, at $c/u_* = 22.7$ (where the orbital velocities are greatest) the minimum surface stress is clearly negative just aft of the crest ($x \sim 1.1$ in figure 24) because of the complex near-surface flow patterns. We should note that for *moving*

waves the presence of negative surface stress is not a clear indicator of flow separation as discussed thoroughly by Gent & Taylor (1977). Close inspection of the near-surface average streamlines (not presented) shows no hint of flow separation in this case: the average streamlines smoothly follow the wave surface. The appearance of the negative surface stress near the crest is a consequence of the sharp vertical change in the u velocity field. As noted previously (see § 7.7), just aft of the crest the u-component of the surface orbital velocity is positive but at the same streamwise location just slightly above the surface the wave-induced velocity perturbation is negative. As a result the u velocity profile, in a coordinate system moving with the wave phase speed, has an elevated local minimum which results in a negative surface stress.

8. Conclusions

A numerical scheme that utilizes co-located differencing and a conformal transformation can be successfully applied to the direct numerical simulation (DNS) of turbulent flow over idealized moving sinusoidal waves. The use of cell-centred Cartesian velocity components as fundamental unknowns coupled with contravariant flux velocity components at the cell faces simplifies the advective operators and makes the co-located scheme attractive for flows with complex geometries. Our numerical results reproduce analytic solutions for two-dimensional laminar flow over a stationary small-wave-slope sinusoidal waveform. Computations of plane turbulent Couette flow with flat boundaries are in good agreement with existing laboratory results and other numerical simulations.

Simulations of turbulent flow over two-dimensional moving water waves were carried out at a wall Reynolds number $Re_* = 130$. In the present idealization, the wave shape and associated orbital velocities are imposed, i.e. the waves do not evolve under the action of the wind. The results show that the waves significantly influence the mean flow, vertical momentum fluxes, velocity variances, pressure, and form stress (drag) depending on wave age c/u_* (ratio of wave speed to wall friction velocity) and wave slope ak. At low values of $c/u_* < 14$ moving waves increase the form stress (or drag) compared to a stationary wave, while at $c/u_* > 14$ the form stress changes sign and acts to drive the wind.

The mean vertical velocity profiles in the presence of waves obey the log-linear form $u/u_* = 1/\kappa \ln z/z_o$ but the von Kármán constant κ and roughness length z_o depend on c/u_* and ak. z_o is maximum for $c/u_* = 7.8$ while for fast moving waves the roughness length is only slightly larger than for a smooth flat boundary. Consistent with the increased surface roughness, the mean velocity profiles display shorter buffer and longer logarithmic regions at small c/u_*. The variation of z_o with wave age is a consequence of the sign change of the surface form stress since the surface drift velocity is identically zero. Also, we found that waves tend to reduce κ by slightly more than 10%. Turbulence statistics show that the wave-correlated effects depend on wave age and wave slope but are primarily confined to a region $kz < 1$ (where k is the wavenumber of the surface undulation and z is the vertical coordinate); the turbulent momentum flux is altered by as much as 40% depending on the combination of ak and c/u_*.

In general the mean flow tends to follow the undulating moving wavy surface. A region of closed streamlines (or cat's-eye pattern) centred about the critical layer height was found to be dynamically important at low to moderate values of c/u_*. At small c/u_*, the centre of the cat's-eye first forms slightly upwind of the trough and close to the undulating surface. With increasing c/u_*, the cat's-eye pattern thickens

and moves upstream of the wave trough. At $c/u_* = 11.5$, the centre of the cat's-eye forms well above the surface and only slightly influences the flow patterns. The presence of slow moving fluid in the cat's-eye causes the mean streamlines to be deflected away from the moving wavy surface.

Contours of wave-correlated velocity and flux fields also are strongly dependent on the variation of the critical layer height z_{cr} and to a lesser extent the surface orbital velocities. Above the critical layer the positions of the maximum and minimum wave-correlated vertical velocity w_w depend on the shape of the critical layer: the maximum and minimum in w_w occur upwind and downwind of the peak in z_{cr}, like a stationary surface. The variation of the horizontal wave-correlated field u_w is more tightly coupled to conditions above and below the critical layer height. The wave-correlated flux $u_w w_w$ is positive (negative) above (below) the critical layer height.

REFERENCES

ANDERSON, D. A., TANNEHILL, J. C. & PLETCHER, R. H. 1984 *Computational Fluid Mechanics and Heat Transfer.* McGraw Hill.

ARAKAWA, A. 1966 Computational design for long-term numerical integration of the equations of fluid motion: I. Two-dimensional incompressible flow. *J. Comput. Phys.* **1**, 119–143.

AYDIN, E. M. & LEUTHEUSSER, H. J. 1991 Plane-Couette flow between smooth and rough walls. *Exps. Fluids* **11**, 302–312.

BECH, K., TILLMARK, N., ALFREDSSON, P. H. & ANDERSSON, H. I. 1995 An investigation of turbulent plane Couette flow at low Reynolds numbers. *J. Fluid Mech.* **286**, 291–325.

BELCHER, S. E. & HUNT, J. C. R. 1998 Turbulent flow over hills and waves. *Ann. Rev. Fluid Mech.* **30**, 507–538.

BENJAMIN, T. B. 1959 Shearing flow over a wavy boundary. *J. Fluid Mech.* **6**, 161–205.

CAPONI, E. A., FORNBERG, B., KNIGHT, D. D., MCLEAN, J. W., SAFFMAN, P. G. & YUEN, H. C. 1982 Calculations of laminar viscous flow over a moving wavy surface. *J. Fluid Mech.* **124**, 347–362.

CHERUKAT, P., NA, Y., HANRATTY, T. J. & MCLAUGHLIN, J. B. 1998: Direct numerical simulation of a fully developed turbulent flow over a wavy wall. *Theor. Comput. Fluid Dyn.* **11**, 109–134.

CHOI, H., MOIN, P. & KIM, J. 1992 Direct numerical simulation of turbulent flow over riblets. *Center for Turbulence Research Stanford University, CTR manuscript* 137.

DE ANGELIS, V., LOMBARDI, P. & BANERJEE, S. 1997 Direct numerical simulation of turbulent flow over a wavy wall. *Phys. Fluids* **9**, 2429–2442.

EDSON, J. B. & FAIRALL, C. W. 1998 Similarity relationships in the marine atmospheric surface layer for terms in the TKE and scalar variance budgets. *J. Atmos. Sci.* **55**, 2311–2328.

EINAUDI, F., FINNIGAN, J. J. & FUA, D. 1984 Gravity wave turbulence interaction in the presence of a critical level. *J. Atmos. Sci.* **41**, 661–667.

FERZIGER, J. H. & PERIĆ, M. 1996 *Computational Methods for Fluid Dynamics.* Springer.

GENT, P. R. 1977 A numerical model of the air flow above water waves. Part 2. *J. Fluid Mech.* **82**, 349–369.

GENT, P. R. & TAYLOR, P. A. 1976 A numerical model of the air flow above water waves. *J. Fluid Mech.* **77**, 105–128.

GENT, P. R. & TAYLOR, P. A. 1977 A note on 'separation' over short wind waves. *Boundary-Layer Met.* **11**, 65–87.

GONG, W., TAYLOR, P. A. & DORNBRACK, A. 1996 Turbulent boundary-layer flow over fixed aerodynamically rough two-dimensional sinusoidal waves. *J. Fluid Mech.* **312**, 1–37.

GOTTLIEB, D. & ORSZAG, S. A. 1977 *Numerical Analysis of Spectral Methods: Theory and Applications.* SIAM-CBMS Monograph, vol. 26.

HARRIS, J. A. & STREET, R. L. 1994 Numerical simulation of turbulent flow over a moving wavy boundary: Norris and Reynolds extended. *Phys. Fluids* **6**, 924–943.

HARRIS, J. A., BELCHER, S. E. & STREET, R. L. 1996 Linear dynamics of wind waves in coupled turbulent air–water flow. Part 2. Numerical model. *J. Fluid Mech.* **308**, 219–254.

HENN, D. S. & SYKES, R. I. 1999 Large-eddy simulation of flow over wavy surfaces. *J. Fluid Mech.* **383**, 75–112.

HRISTOV, T., FRIEHE, C. & MILLER, S. 1998 Wave-coherent fields in airflow over ocean waves: Identification of cooperative behavior buried in turbulence. *Phys. Rev. Lett.* **81**, 5245–5248.

HRISTOV, T., FRIEHE, C., MILLER, S. & J. EDSON, J. 1999 Identification and analysis of wind-wave interactions in field experiment data. *13th Symp. Boundary Layers and Turbulence, Dallas, TX*, pp. 233–236. Am. Met. Soc. (preprint)

HSU, C.-T. & HSU, E. Y. 1983 On the structure of turbulent flow over a progressive water wave: theory and experiment in a transformed, wave-following co-ordinate system. Part 2. *J. Fluid Mech.* **131**, 123–153.

HSU, C.-T., HSU, E. Y. & STREET, R. L. 1981 On the structure of turbulent flow over a progressive water wave: theory and experiment in a transformed, wave-following co-ordinate system, *J. Fluid Mech.* **105**, 87–117.

HUSSAIN, A. K. M. F. & REYNOLDS, W. C. 1970 The mechanics of an organized wave in turbulent shear flow. *J. Fluid Mech.* **41**, 241–258.

KENDALL, J. M. 1970 The turbulent boundary layer over a wall with progressive surface waves. *J. Fluid Mech.* **41**, 259–281.

KIM, J., MOIN, P. & MOSER, R. 1987 Turbulence statistics in fully developed channel flow at low Reynolds number. *J. Fluid Mech.* **177**, 133–166.

KITAIGORODSKII, S. A. & DONELAN, M. A. 1984 Wind–wave effects on gas transfer. In *Gas Transfer at Water Surfaces* (ed. W. Brutsaert & G. H. Jirka). Reidel.

KOMMINAHO, J., LUNDBLADH, A. & JOHANSSON, A. V. 1996 Very large structures in plane turbulent Couette flow. *J. Fluid Mech.* **320**, 259–285.

KRETTENAUER, K & SCHUMANN, U. 1992 Numerical simulation of turbulent convection over wavy terrain. *J. Fluid Mech.* **237**, 261–299.

LE, H. & MOIN, P. 1991 An improvement of fractional step methods for the incompressible Navier–Stokes equations. *J. Comput. Phys.* **92**, 369–379.

LEE, M. J. & KIM, J. 1991 The structure of turbulence in a simulated plane Couette flow. In *Eighth Symp. on Turbulent Shear Flows, Tech. University of Munich*, pp. 5.3.1–5.3.6.

LI, P. Y. 1995 A numerical study on energy transfer between turbulent air flow and finite amplitude water waves. PhD Thesis, York University.

LIGHTHILL, M. J. 1962 Physical interpretation of the mathematical theory of wave generation by wind. *J. Fluid Mech.* **14**, 385–398.

LIGHTHILL, M. J. 1978 *Waves in Fluids.* Cambridge University Press.

MAASS, C. & SCHUMANN, U. 1994 Numerical simulation of turbulent flow over a wavy boundary. *Proc. First ERCOFTAC Workshop on Direct and Large-Eddy Simulation*, pp. 287–297.

MASTENBROEK, C. 1996 Wind-wave interaction. PhD Thesis, Delft Tech. Univ.

MASTENBROEK, C., MAKIN, V. K., GARAT, M. H. & GIOVANANGELI, J. P. 1996 Experimental evidence of the rapid distortion of turbulence in the air flow over water waves. *J. Fluid Mech.* **318**, 273–302.

MCWILLIAMS, J. C., SULLIVAN, P. P. & MOENG, C.-H. 1997 Langmuir turbulence in the ocean. *J. Fluid Mech.* **334**, 1–30.

MILES, J. W. 1957 On the generation of surface waves by shear flows. *J. Fluid Mech.* **3**, 185–204.

MOBELY, C. D. & STEWART, R. J. 1980 On the numerical generation of boundary-fitted orthogonal curvilinear coordinate systems. *J. Comput. Phys.* **34**, 124–135.

MOENG, C.-H. 1984 A large-eddy-simulation model for the study of planetary boundary-layer turbulence. *J. Atmos. Sci.* **41**, 2052–2062.

MOIN, P. & MAHESH, K. 1998 Direct numerical simulation: A tool in turbulence research. *Ann. Rev. Fluid Mech.* **30**, 539–578.

MORINISHI, Y., LUND, T. S., VASILYEV, O. V. & MOIN, P. 1998 Fully conservative higher order finite difference schemes for incompressible flow. *J. Comput. Phys.* **143**, 90–124.

PAPADIMITRAKIS, Y. A., STREET, R. L. & HSU, E. Y. 1988 The bursting sequence in the turbulent boundary layer over progressive, mechanically generated water waves. *J. Fluid Mech.* **193**, 303–345.

PAPAVASSILIOU, D. V. & HANRATTY, T. J. 1997 Interpretation of large-scale structures observed in a turbulent plane Couette flow. *Intl J. Heat Fluid Flow* **18**, 55–69.

RHIE, C. M. & CHOW, W. L. 1983 A numerical study of the turbulent flow past an isolated airfoil with trailing edge separation. *AIAA J.* **21**, 1525–1532.

ROGALLO, R. S. & MOIN, P. 1984 Numerical simulation of turbulent flows. *Ann. Rev. Fluid Mech.* **16**, 99–137.

ROSENFELD, M., KWAK, D. & VINOKUR, M. 1991 A fractional step solution method for the unsteady incompressible Navier–Stokes equations in generalized coordinate systems. *J. Comput. Phys.* **94**, 102–137.

SPALART, P. R., MOSER, R. D. & ROGERS, M. M. 1991 Spectral methods for the Navier–Stokes equations with one infinite and two periodic dimensions. *J. Comput. Phys.* **96**, 297–324.

SULLIVAN, P. P., MCWILLIAMS, J. C. & MOENG, C.-H. 1996 A grid nesting method for large-eddy simulation of planetary boundary-layer flows. *Boundary-Layer Met.* **80**, 167–202.

TAKEUCHI, K., LEAVITT, E. & CHAO, S. P. 1977 Effects of water waves on the structure of turbulent shear flow. *J. Fluid Mech.* **80**, 535–559.

TOWNSEND, A. A. 1972 Flow in a deep turbulent boundary layer over a surface distorted by water waves. *J. Fluid Mech.* **55**, 719–735.

YAGLOM, A. M. 1979 Similarity laws for constant-pressure and pressure-gradient turbulent wall flows. *Ann. Rev. Fluid Mech.* **11**, 505–540.

ZANG, T. A. 1991 On the rotation and skew-symmetric forms for incompressible flow simulations. *Appl. Numer. Maths* **7**, 27–40.

ZANG, Y., STREET, R. L. & KOSEFF, J. R. 1994: A non-staggered grid, fractional step method for time-dependent incompressible Navier–Stokes equations in curvilinear coordinates. *J. Comput. Phys.* **114**, 18–33.